

**Technical Report
TR-1108**

Distribution Models for Optical Scintillation Due to Atmospheric Turbulence

**R.R. Parenti
R.J. Sasiela**

12 December 2005

Lincoln Laboratory
MASSACHUSETTS INSTITUTE OF TECHNOLOGY
LEXINGTON, MASSACHUSETTS



Prepared for the Department of the Air Force under Contract FA8721-05-C-0002.

Approved for public release; distribution is unlimited.

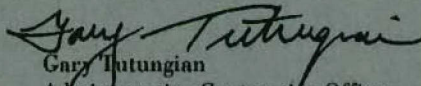
This report is based on studies performed at Lincoln Laboratory, a center for research operated by Massachusetts Institute of Technology. This work was sponsored by the Department of the Air Force under Contract FA8721-05-C-0002.

This report may be reproduced to satisfy needs of U.S. Government agencies.

The ESC Public Affairs Office has reviewed this report, and it is releasable to the National Technical Information Service, where it will be available to the general public, including foreign nationals.

This technical report has been reviewed and is approved for publication.

FOR THE COMMANDER


Gary Tutungian
Administrative Contracting Officer
Plans and Programs Directorate
Contracted Support Management

Non-Lincoln Recipients

PLEASE DO NOT RETURN

Permission has been granted to destroy this document, when it is no longer needed.

Massachusetts Institute of Technology
Lincoln Laboratory

**Distribution Models for Optical Scintillation
Due to Atmospheric Turbulence**

*R.R. Parenti
R.J. Sasiela
Group 107*

Technical Report 1108

12 December 2005

Approved for public release; distribution is unlimited.

ABSTRACT

Traditional analyses of optical scintillation usually invoke the Rytov approximation and the associated assumptions regarding weak phase perturbations throughout the propagation channel. Associated with that approach is the prediction that the statistics of scintillation will be log-normal. This report, which uses the Fresnel propagation function as a basis, challenges many of the standard descriptions of far-field irradiance fluctuations. A key finding of this study is the importance of the ratio between the transmitted beam diameter and the turbulence coherence diameter. Turbulence-induced beam jitter is found to be a dominant effect when this ratio is close to unity, and the relationship between pointing error and scintillation is examined in detail. As a result of this work, models for the mean Strehl, scintillation index, and signal-fade distributions have been developed. Included in this document are a set of detailed comparisons between the new theoretical models and numerical results derived from a beamwave propagation code developed by Lincoln Laboratory.

ACKNOWLEDGMENTS

The authors are pleased to acknowledge the collaboration of Profs. Larry C. Andrews (University of Central Florida) and Ronald L. Phillips (University of Central Florida and the Kennedy Space Center) in the investigation of scintillation effects documented in this report. This interaction included frequent discussions and meetings over a two-year period.

Acknowledgment is also gratefully given for the efforts of Dr. Scot Shaw and Mr. Steven Michael, who wrote and maintain the POPS wavefront propagation code that is the source of all of the simulation data used in this study.

TABLE OF CONTENTS

Abstract	iii
Acknowledgments	v
List of Illustrations	ix
1. INTRODUCTION	1
2. THE RYTOV APPROXIMATION FOR WEAK PERTURBATIONS	3
3. THE THREE STAGES OF OPTICAL SCINTILLATION	7
4. A NEW PERSPECTIVE ON THE BEAMWAVE SCINTILLATION PROBLEM	11
4.1 Beamwave Propagation Relationships for Unperturbed Gaussian Beams	11
4.2 Receiver-Plane Field Effects Due to Near-Field Phase Perturbations	17
4.3 Receiver-Plane Field Effects Due to Far-Field Phase Perturbations	18
4.4 Numerical Simulation Tools	23
5. IRRADIANCE STATISTICS AT THE RECEIVER-PLANE BORESIGHT	25
5.1 Scintillation Index for $w_0/r_0 \ll 1$: Weak Far-Field Turbulence	25
5.2 Scintillation Index for $w_0/r_0 \approx 1$: Moderate Near-Field Turbulence	30
5.3 Scintillation Index for $w_0/r_0 \gg 1$: Saturation Due to Strong Near-Field Turbulence	35
5.4 Combining the Scintillation Index Models	37
5.5 Strehl Ratio Models	40
6. RECEIVER-PLANE IRRADIANCE DISTRIBUTION MODELS	43
6.1 Distribution Model for $w_0/r_0 \ll 1$: Weak Far-Field Turbulence	43
6.2 Distribution Model for $w_0/r_0 \approx 1$: Moderate Near-Field Turbulence	44
6.3 Distribution Model for $w_0/r_0 \gg 1$: Saturation Due to Strong Near-Field Turbulence	52
6.4 Combining the Irradiance Distribution Models	54
7. CONCLUSIONS	57
APPENDIX	59
REFERENCES	63

LIST OF ILLUSTRATIONS

Figure No.		Page
3-1	Estimates of σ_{χ}^2 as a function of the normalized field perturbation strength for vertical path propagation. These results were obtained from numerical simulations of beamwave projection through a series of discrete phase screens from a ground-level transmitter to a receiver in geostationary orbit. In the small D/r_0 limit these data agree with the Rytov prediction for point-source scintillation.	8
3-2	Beam profile evolution as a function of the normalized field perturbation strength. These images indicate three distinct physical mechanisms for irradiance fluctuations in the plane of the receiver. The tilt-jitter effects and beam breakup shown in the second and third images are not accounted for by the Rytov theory.	9
4-1	Evolution of a focused-beam profile from transmitter to receiver planes. The shape of the beam is governed by geometrical propagation in the near-field of the transmitter and by diffractive spreading in the far field. The transition between these two regions occurs at the Rayleigh range.	12
4-2	Illustration of the effect of placing a focusing element in the far-field of a point source. A point along the propagation axis will experience an increase or decrease in the optical irradiance, depending on the sign of the focusing element. Note that phase distortions that result in an on-axis irradiance enhancement only occur in the far field of the transmitter.	19
4-3	Comparison of the integrals of $\cos(x^2)$ and $\sin(x^2)$ with the integral of the rectangle function.	22
5-1	Far-field beam image (left figure) and horizontal-axis profile (right figure) for $w_0/r_0 = 0.01$. The Hufnagel-Valley turbulence profile was used in this simulation of vertical propagation, which resulted in an r_0 value of 19 cm at 1.55 μm . The propagation distance is 40 Mm, and the linear dimension of the image fields is 50 km. The long-exposure beam profile is approximately diffraction-limited.	26

LIST OF ILLUSTRATIONS (Continued)

Figure No.		Page
5-2	Comparison of simulation results (red and blue data points) with the model for turbulence concentrated in the far-field of the transmitter (blue dashed line). The upper figure represents an uplink geometry and the lower is horizontal propagation to 10 km.	29
5-3	Far-field beam image (left figure) and horizontal-axis profile (right figure) for $w_0/r_0 = 1$. The Hufnagel-Valley turbulence profile was used in this simulation of vertical propagation, which resulted in an r_0 value of 19 cm at 1.55 μm . The propagation distance is 40 Mm, and the linear dimension of the image field is 1 km.	30
5-4	Comparison of simulation results (red and blue data points) with the transition-region scintillation models (dashed lines). The upper figure represents an uplink geometry and the lower is horizontal propagation to 10 km.	34
5-5	Far-field beam image (left figure) and horizontal-axis profile (right figure) for $w_0/r_0 = 5$. The Hufnagel-Valley turbulence profile was used in this simulation of vertical propagation, which resulted in an r_0 value of 19 cm at 1.55 μm . The propagation distance is 40 Mm, and the linear dimension of the image fields is 1 km. The average dimension of the individual speckles is approximately diffraction-limited.	35
5-6	Comparison of simulation results (red and blue data points) with the composite scintillation index models (dashed lines). The upper figure represents an uplink geometry and the lower is horizontal propagation to 10 km.	39
5-7	Comparison of simulation results (red and blue data points) with the Strehl ratio models (dashed lines). The upper figure represents an uplink geometry and the lower is horizontal propagation to 10 km.	41
6-1	Comparison of uplink simulation results for $w_0/r_0 = 0.0744$ (black data points) with the log-normal distribution model (red line). The upper figure represents the tilt-corrected turbulence case and the lower is the uncorrected case.	45

LIST OF ILLUSTRATIONS (Continued)

Figure No.		Page
6-2	Comparison of uplink simulation results for $w_0/r_0 = 0.187$ (black data points) with the log-normal distribution model (red line). The upper figure represents the tilt-corrected turbulence case and the lower is the uncorrected case.	49
6-3	Comparison of uplink simulation results for $w_0/r_0 = 0.371$ (black data points) with the log-normal distribution model (red line). The upper figure represents the tilt-corrected turbulence case and the lower is the uncorrected case.	50
6-4	Comparison of uplink simulation results for $w_0/r_0 = 0.930$ (black data points) with the log-normal distribution model (red line). The upper figure represents the tilt-corrected turbulence case and the lower is the uncorrected case.	51
6-5	Comparison of uplink simulation results for $w_0/r_0 = 3.72$ (black data points) with the negative-exponential distribution model (red line). The upper figure represents the tilt-corrected turbulence case and the lower is the uncorrected case.	53
6-6	Comparison of uplink simulation results for the tilt-corrected beam (black data points) with the composite distribution model (green line). The upper figure represents the $w_0/r_0 = 0.187$ case and the lower is the result for $w_0/r_0 = 0.371$.	55

1. INTRODUCTION

Scintillation effects due to electromagnetic wave propagation through an inhomogeneous medium are generally treated as a weak perturbation of the vacuum solution to Maxwell's electromagnetic field equations. When this approach is combined with a statistical description of turbulence-induced refractive index fluctuations, one can accurately model the behavior of far-field irradiance fluctuations when the path-integrated wavefront distortion is small compared to the optical wavelength. Although many investigators have also applied this analytical approach to strong turbulence conditions, the results of this study demonstrate that better descriptions of the scintillation phenomenon result when the propagation expressions are modified to permit a wider range of validity.

The need for a nontraditional description of optical scintillation is immediately apparent to anyone who has carefully studied beam images generated by numerical simulations or experiments in which laser beams are propagated through an atmospheric channel. The compositional evolution of the short-exposure beam profile is dramatic as the strength of the field perturbations increases, and therefore no single description adequately characterizes the entire range of behavior. This report identifies three distinct performance regimes and derives separate statistical models for each.

This study is primarily focused on the development of better link-budget models for free-space optical communication systems, but the derived results are applicable to a wide range of propagation scenarios. The statistical descriptions developed thus far only relate to uncorrelated path realizations. Time-dependent behavior will be addressed in this next phase of this investigation.

2. THE RYTOV APPROXIMATION FOR WEAK PERTURBATIONS

To establish an historical perspective for the new work discussed in subsequent sections, it will be useful to briefly review the standard assumptions and predictions that derive from the application of the Rytov perturbation theory. The Rytov approximation is described in a variety of texts; the following derivation is extracted from Goodman [1].

At any point in space the optical field, U , must satisfy Maxwell's equation

$$\nabla^2 U + \frac{\omega^2 n^2}{c^2} U = 0 \quad , \quad (2-1)$$

where ω is the angular frequency, n is the refractive index, and c is the speed of light. For an inhomogeneous medium, the refractive index can be divided into a constant term, n_0 , and a perturbation, n_1 , that will vary in space and time. The expression for the perturbed field, \tilde{U} , is

$$\nabla^2 (U + U_\varepsilon) + \frac{\omega^2}{c^2} (n + n_\varepsilon)^2 (U + U_\varepsilon) = 0 \quad , \quad (2-2)$$

where U and U_ε are the unperturbed and perturbation field components, respectively. For atmospheric propagation, n can be set to unity without loss of generality. If n_ε is small compared to unity, then the following expression will be valid

$$\nabla^2 U_\varepsilon + k^2 U_\varepsilon = -2k^2 n_\varepsilon U \quad , \quad (2-3)$$

where $k = \omega/c = 2\pi/\lambda$ and λ is the optical wavelength. For plane-wave propagation through frozen turbulence, the solution to Eq. (2-3) can be expressed as a three-dimensional coherent integral over the entire scattering volume

$$U_\varepsilon(\vec{r}) = \frac{1}{4\pi} \int_V \frac{\exp\{ik|\vec{r} - \vec{r}'|\}}{|\vec{r} - \vec{r}'|} \left[2k^2 n_\varepsilon(\vec{r}') U(\vec{r}') \right] d^3\vec{r}' \quad . \quad (2-4)$$

Goodman notes that the effective scattering angle due to refractive-index fluctuations is very small, in which case the Fresnel approximation can be applied. The separation of the axial and radial components in the free-space Green's function yields the following form for beam propagation along the positive z axis

$$U_{\varepsilon}(\vec{r}) \approx \frac{k^2}{2\pi} \iiint_{x' y' z'} \frac{\exp \left\{ i k \left[(z - z') + \frac{(x - x')^2 + (y - y')^2}{2(z - z')} \right] \right\}}{z - z'} n_{\varepsilon}(\vec{r}') U(\vec{r}') dx' dy' dz'. \quad (2-5)$$

The relationship given in Eq. (2-2) is referred to as the Born approximation, which assumes that the net field value can be represented as the linear sum of the unperturbed field and a set of weak perturbation components. An alternative approach, known as Rytov approximation, defines the complex phase, $\psi = \chi + i\phi$, such that

$$\tilde{U} = \exp\{\tilde{\psi}\} = \exp\{\psi + \psi_{\varepsilon}\}. \quad (2-6)$$

In this approximation the phase perturbation components are assumed to be additive. For weak fluctuations

$$\psi_{\varepsilon} = \ln \left\{ 1 + \frac{U_{\varepsilon}}{U} \right\} \approx \frac{U_{\varepsilon}}{U} \quad (2-7)$$

so that the volume integral can be written as

$$\psi_{\varepsilon}(\vec{r}) \approx \frac{k^2}{2\pi U(\vec{r})} \iiint_{x' y' z'} \frac{\exp \left\{ i k \left[(z - z') + \frac{(x - x')^2 + (y - y')^2}{2(z - z')} \right] \right\}}{z - z'} n_{\varepsilon}(\vec{r}') U(\vec{r}') dx' dy' dz'. \quad (2-8)$$

The real part of this expression specifies the log-amplitude component of the field variations due to inhomogeneities in the refractive-index. The Rytov approximation is more frequently used than the Born approximation and is thought to be more accurate for strong turbulence conditions.

Statistical investigations of scintillation due to refractive index fluctuations in the atmosphere usually begin with an expression similar to that given in Eq. (2-8) and proceed with an analysis based on the spatial frequency properties of the perturbation parameter, n_{ε} . Analytical investigations of this type date back to the work of Kolmogorov [2] and Tatarski [3], and have since been continued by a number of investigators including Ishimaru [4], Strohbehn [5], Fried [6], and Yura [7]. The results of these investigations are typically expressed in terms of complex multidimensional integrals, which are usually evaluated numerically. A more recent technique based on Mellin transforms has been developed by

Sasiela [8], which allows the solutions to many important problems to be represented in closed form. To simplify the mathematics, most analytical calculations are limited to two propagation geometries—irradiation from a point source or an infinite plane wave.

The computational approaches just described have been applied successfully to a wide variety of practical problems, including the design of adaptive-optics correction systems for astronomical imaging and link budget estimation for free-space optical communications. The primary characterization of the atmospheric channel is the C_n^2 profile, which quantifies the strength of the refractive index fluctuations. For many system constructs the mean receiver irradiance and the irradiance variance can be related to the low-order moments of the C_n^2 profile, i.e.,

$$\mu_m \equiv \int_0^L \gamma(z) z^m C_n^2(z) dz , \quad (2-9)$$

where L is the distance between the transmitter and receiver, and γ describes the beam dimensions. The standard result for the variance of χ for point-source radiation propagating from ground to a receiver in space at range L is

$$\sigma_\chi^2 \approx 0.563 k^{7/6} \mu_{5/6} , \quad (2-10)$$

and for an infinite plane wave traversing the same path

$$\sigma_\chi^2 \approx 0.563 k^{7/6} \mu_0 L^{5/6} . \quad (2-11)$$

Based on the central limit theorem it is usually argued that both ϕ and χ are Gaussian random variables, in which case Eq. (2-7) specifies that the field amplitude statistics will be log-normal.

Despite the success of the Rytov theory and related mathematical approximations, there are many interesting beam-propagation scenarios that cannot be accurately analyzed in this manner. The relationship given in Eq. (2-11) is immediately suspect, since it predicts that σ_χ^2 will become infinite as $L \rightarrow \infty$. This result is inconsistent with simulations of large-diameter transmitters, which show that σ_χ^2 approaches a constant as the propagation range becomes large.

Transmission from apertures of finite dimension is known as beamwave propagation, and for many geometries of interest the associated scintillation properties are not well characterized by relationships derived for the point-source or infinite plane-wave cases. Furthermore, numerical simulations and field experiments both demonstrate that the statistics of fading due to propagation through strong turbulence are not log-normal. In short, many of the assumptions commonly applied to the design of systems subject to strong channel fluctuations are inappropriate and may lead to serious errors in performance estimates.

3. THE THREE STAGES OF OPTICAL SCINTILLATION

The optical field relationships given in Eqs. (2-7) and (2-8) suggest a multiplicative process that imposes a weak distortion onto a diffraction-limited beam profile. Numerical simulations (which are described later in this document) verify this prediction when the integral of the C_n^2 profile over the propagation path is small. A good measure of the absolute turbulence strength is the coherence diameter, r_0 , defined by Fried [9]

$$r_0 = \left[0.423 k^2 \int_0^L C_n^2(z) dz \right]^{-3/5} . \quad (3-1)$$

It can be shown that the relative impact of the atmosphere on the far-field quality of a beam transmitted from an aperture of diameter D is directly related to the D/r_0 ratio. This quantity plays a primary role in the characterization of scintillation behavior.

Charnotskii [10] was one of the first investigators to propose a segmented classification of scintillation based on a multidimensional parameter space, and his article suggests that as many as 11 distinct classes are needed to properly describe all aspects of this complex phenomenon. Charnotskii's research is unique in that it concludes that a thorough analysis of scintillation cannot be based solely on a single set of weak-turbulence approximations. One would hope, however, that it might be possible to capture the essential aspects of this process in a somewhat simpler set of mathematical constructs.

The phenomenological approach proposed in this document segregates scintillation behavior into three classes, and associates each class with a single observable—the D/r_0 ratio. This methodology derives from a detailed analysis of vertical-path and horizontal-path numerical simulations performed at Lincoln Laboratory. On a qualitative level these new results are consistent with the work of prior investigators, and the predicted numerical values for very weak and very strong turbulence conditions were correctly reproduced. (Contrary to the prediction that obtains from Eq. (2-11), σ_χ^2 achieves a saturation value of 0.25 for severe channel conditions.) When σ_χ^2 is plotted as a function of D/r_0 , a clear trend is revealed. As shown in Figure 3-1, for a scenario in which the r_0 value is fixed, the log-amplitude variance is constant when $D/r_0 \ll 1$ and approaches the saturation limit when $D/r_0 \gg 1$. The transition region occurs when D/r_0 is in the range of 1 to 10. This behavior has been observed for a variety of turbulence profiles and for both vertical and horizontal-path geometries.

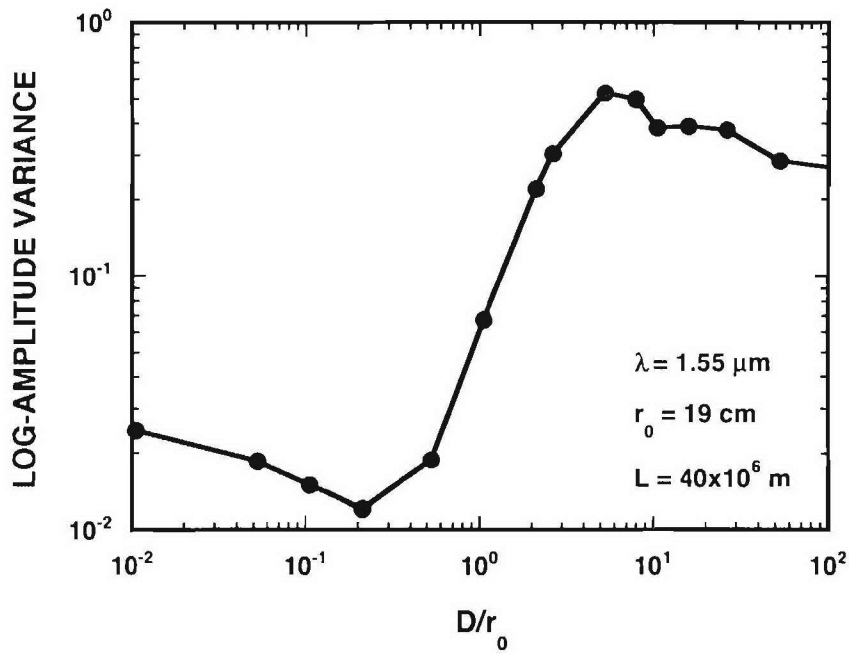


Figure 3-1. Estimates of σ_χ^2 as a function of the normalized field perturbation strength for vertical path propagation. These results were obtained from numerical simulations of beamwave projection through a series of discrete phase screens from a ground-level transmitter to a receiver in geostationary orbit. In the small D/r_0 limit these data agree with the Rytov prediction for point-source scintillation.

While plots similar to that shown in Figure 3-1 have frequently been published, little attention has been paid to the physical processes that shape the scintillation curve beyond the region where the Rytov approximation is applicable. A detailed examination of far-field beam images derived from numerical simulations reveals clear distinctions between the profiles for small, intermediate, and large values of D/r_0 ; these differences are illustrated by the examples shown in Figure 3-2. The short-exposure image shown in the leftmost picture indicates the behavior when D/r_0 is small. In this case the long-exposure beam width is approximately diffraction-limited, but individual realizations display a relatively weak multiplicative noise component. This is the only region in which the Rytov approximation is strictly valid and for which the distribution of intensity fluctuations is log-normal.

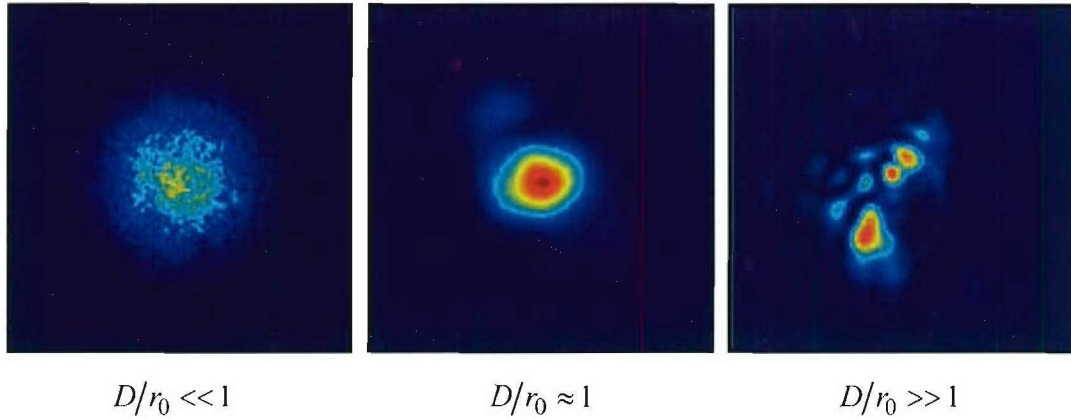


Figure 3-2. Beam profile evolution as a function of the normalized field perturbation strength. These images indicate three distinct physical mechanisms for irradiance fluctuations in the plane of the receiver. The tilt-jitter effects and beam breakup shown in the second and third images are not accounted for by the Rytov theory.

When D/r_0 is of order unity, the strength of the log-normal fluctuations begins to diminish, and the scale size of the noise peaks becomes comparable to the diffraction-limited beam diameter. However, tilt jitter becomes more pronounced, and low spatial-frequency aberrations distort the short-exposure beam shape. Both of these effects result in a dramatic increase in far-field irradiance fluctuations. Although gross beam motion is not usually thought of as scintillation, the distinction is artificial since both introduce a corruption of the on-target irradiance. The statistical properties for this case are not log-normal and are strongly dependent on the quality of the track correction used in the transmitter.

Tilt fluctuations are associated with the appearance of the lowest spatial-frequency phase-distortion components, which are the dominant distortion factor [11]. As the strength of the higher spatial-frequency constituents becomes comparable to 2π , the beam sidelobes increase in intensity until the mainlobe and the sidelobes become indistinguishable. Full saturation occurs when the phase errors across the aperture are uniformly distributed between $-\pi$ and π . Negative-exponential statistics are observed for these conditions.

The statistical descriptions developed in the following sections are a direct product of observations drawn from Figures 3-1 and 3-2. The intent of this effort is to develop a better understanding of the causes and the effects of atmospheric turbulence beyond the range in which the Rytov approximation is valid. The goal is to provide a set of mathematical constructs that can be used to predict system performance for any propagation geometry and turbulence environment.

4. A NEW PERSPECTIVE ON THE BEAMWAVE SCINTILLATION PROBLEM

The most important observation made in the previous section is that the Rytov approximation fails for the scenarios of greatest concern to the designers of free-space optical systems that are intended to function in a stressing turbulence environment. Even a cursory analysis of numerical results for moderate to strong perturbations reveals serious discrepancies between predictions and measurements. To develop improved performance models, the effects of tilt jitter and beam breakup must be explicitly incorporated.

In the investigation of this problem, it was soon realized that diffraction plays a key role in beamwave scintillation. The location of the perturbation field relative to the Rayleigh range, where diffractive beam spreading becomes important, strongly impacts the strength and statistical behavior of signal fluctuations measured at the receiver plane. It is common to refer to field points that are within the Rayleigh range, $z_R = D^2/\lambda$, as being in the near field of the transmitter, and describe more distant points as lying in the far field. For the case of beam propagation from a large transmitter from ground to space, turbulence-induced distortions will be solely confined to the near field of the source. As the transmitter diameter shrinks, the Rayleigh range moves closer to the source and the accumulated perturbations migrate to the far field. In the first example, the fields in the receiver and transmitter planes form a simple Fourier-conjugate pair. A quantitative description of the latter case is significantly more complex, and this difference is central to the discussions that follow.

Although this analysis is intended to be as general as possible, three simplifying constraints will be applied that are applicable to most system constructs of practical utility. The first is that the receiver aperture is small compared to the size of the speckle features in the far-field beam and that it lies along the nominal propagation path. This assumption enables scintillation analyses to be performed on a single point within the plane of the receiver. The second constraint is that the receiver lies at the focus of the transmitted beam. For most systems of practical interest, the average received irradiance is maximized when the focus applied to the transmitted beam is equal to the receiver range; in addition, this geometry also establishes an exact Fourier-transform relationship between the two optical planes. The third assumption is that the transmitted beam is an infinite Gaussian characterized by the field radius, w_0 . Although much of the turbulence literature assumes transmission from a uniformly-illuminated aperture of diameter D , the beams from most transceivers are best described by a truncated-Gaussian shape. It will be shown that relationships developed for uniformly-illuminated apertures can be easily converted to Gaussian-beam expressions through the application of the scaling transformation, $D = 2^{3/2} w_0$.

4.1 BEAMWAVE PROPAGATION RELATIONSHIPS FOR UNPERTURBED GAUSSIAN BEAMS

The evolution of the beamwave profile with propagation range is shown graphically in Figure 4-1. The spatial and temporal characteristics of irradiance fluctuations resulting from perturbations introduced in the near- and far-field regions of the beam differ significantly, and it is necessary to develop a separate

set of analytical tools for each region. The basic mathematical relationships that are later used to construct statistical irradiance models are developed in this section.

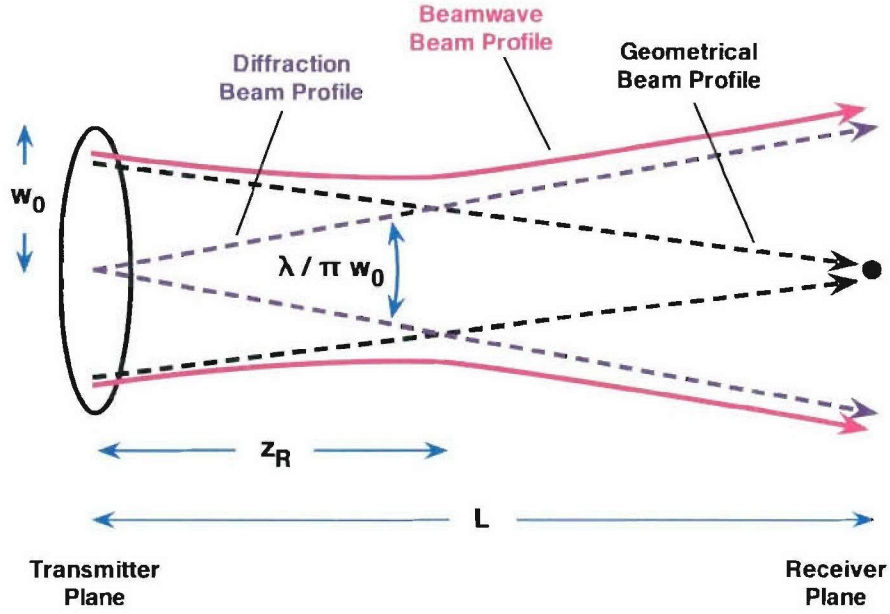


Figure 4-1. Evolution of a focused-beam profile from transmitter to receiver planes. The shape of the beam is governed by geometrical propagation in the near-field of the transmitter and by diffractive spreading in the far field. The transition between these two regions occurs at the Rayleigh range.

The composite beamwave profile shown in Figure 4-1 shows that the shape of the focused beam is established by the geometrical propagation pattern in the transmitter's near-field region, but becomes diffraction-limited in the far-field. A Gaussian beam of infinite extent remains Gaussian over the entire range and is completely characterized by the range dependent radius, $w(r)$, and wavefront focal radius, $f(r)$. The following derivation borrows heavily from Goodman's discussion of Fresnel propagation [12].

The expression for the optical field amplitude in the plane perpendicular to the propagation direction derives from the Huygens-Fresnel principle

$$U_1(x_1, y_1) = \int_{-\infty}^{\infty} \int_{-\infty}^{\infty} h(x_0, y_0; x_1, y_1) U_0(x_0, y_0) dx_0 dy_0 \quad , \quad (4-1)$$

where U_0 is the complex field amplitude within the x, y plane at range z_0 , and U_l is the amplitude at z_l . The propagation transfer function, h , is given by

$$h(x_0, y_0; x_1, y_1) \approx -\frac{ik}{2\pi(z_1 - z_0)} \exp\left\{ik \sqrt{(x_1 - x_0)^2 + (y_1 - y_0)^2 + (z_1 - z_0)^2}\right\}, \quad (4-2)$$

where $k = 2\pi/\lambda$. For most problems of interest $(z_1 - z_0)^3 \gg \frac{\pi}{4\lambda} \left[(x_1 - x_0)^2 + (y_1 - y_0)^2 \right]_{\max}^2$, in which case the Fresnel approximation is applicable

$$h(x_0, y_0; x_1, y_1) \approx -\frac{ik \exp\{ik(z_1 - z_0)\}}{2\pi(z_1 - z_0)} \exp\left\{i \frac{k}{2(z_1 - z_0)} \left[(x_1 - x_0)^2 + (y_1 - y_0)^2 \right]\right\}. \quad (4-3)$$

An important property of the Fresnel approximation is that in the absence of field perturbations a single propagation step from z_0 to z_2 yields the same result as multiple steps within the same interval. Consider the two-step process $z_0 \Rightarrow z_1 \Rightarrow z_2$ described by the equation

$$U_2(x_2) = \int_{-\infty}^{\infty} \int_{-\infty}^{\infty} U_0(x_0) \exp\left\{i \frac{k}{2(z_2 - z_1)} (x_2 - x_1)^2\right\} \exp\left\{i \frac{k}{2(z_1 - z_0)} (x_1 - x_0)^2\right\} dx_1 dx_0.$$

Observe that

$$a(x_1 - x_0)^2 + b(x_2 - x_1)^2 = (a+b) \left[x_1 - \frac{ax_0 + bx_2}{a+b} \right]^2 + \frac{ab}{a+b} (x_2 - x_0)^2,$$

where $a = \frac{k}{2(z_1 - z_0)}$ and $b = \frac{k}{2(z_2 - z_1)}$, and note that the integral over x_1 can be performed using the identity

$$\int_{-\infty}^{\infty} \exp\left\{i\alpha(x - \beta)^2\right\} dx = \exp\left\{i\sqrt{\pi/2\alpha}\right\}.$$

This yields the result

$$U_2(x_2) = \exp\left\{i \sqrt{\frac{\pi(z_2 - z_1)(z_1 - z_0)}{k(z_2 - z_0)}}\right\} \int_{-\infty}^{\infty} U_0(x_0) \exp\left\{i \frac{k}{2(z_2 - z_0)} (x_2 - x_0)^2\right\} dx_0.$$

With the exception of the leading phase constant, this is equivalent to the propagation expression for the single-step propagation $z_0 \Rightarrow z_2$.

When the propagation range is extended further such that $z_1 - z_0 \gg \frac{\pi}{\lambda} (x_0^2 + y_0^2)_{\max}$, the Fraunhofer approximation provides an accurate estimate of the transformed field

$$h(x_0, y_0; x_1, y_1) \approx \frac{ik \exp\{-ik(z_1 - z_0)\}}{2\pi(z_1 - z_0)} \exp\left\{-ik \frac{(x_1^2 + y_1^2)}{2(z_1 - z_0)}\right\} \exp\left\{ik \frac{(x_0 x_1 + y_0 y_1)}{(z_1 - z_0)}\right\}. \quad (4-4)$$

Note that aside from phase terms that are independent of x_0 and y_0 , this expression is equivalent to a Fourier transform. Goodman shows that this approximation is also valid for short propagation distances if the transmitted beam is focused at z_1 . It is also worth noting that along the boresight path the field expression for Fraunhofer propagation is proportional to the two-dimensional integral of U_0

$$U_1(0,0) = \frac{k}{2\pi(z_1 - z_0)} \int_{-\infty}^{\infty} \int_{-\infty}^{\infty} U_0(x_0, y_0) dx_0 dy_0, \quad (4-5)$$

which is a useful relationship for numerical calculations.

The field transformation concepts just presented provide a basis for a discussion of the effects of turbulence-induced phase perturbations. An important element of the following analysis is the demarcation between the near field and far field of the transmitted beam and the placement of the perturbation with respect to that transition point. The beamwave problem can be significantly simplified by restricting the discussion to focused Gaussian beams. Investigations by Andrews and Phillips have also concentrated on Gaussian-beam behavior [13].

For virtually all cases of interest, optimal performance is achieved when the geometrical focal distance and the range to the receiver are identical. The field at the transmitter will be defined as follows

$$U_0(r_0) = A_0 \exp\left\{-ikr_0^2/2f_0\right\} \exp\left\{-r_0^2/w_0^2\right\}, \quad (4-6)$$

where w_0 is the field radius and f_0 is the focal distance. Assuming Fresnel propagation from $z_0=0$ to z_1 , the field expression at range z_1 is

$$\begin{aligned}
U_1(r_1) &= -i \frac{k}{z_1} \exp\{i k z_1\} \exp\left\{i \frac{k}{2 z_1} r_1^2\right\} A_0 \int_0^\infty \exp\left\{i \frac{k}{2 z_1} r_0^2\right\} U_0(r_0) r_0 J_0\left\{\frac{k}{z_1} r_0 r_1\right\} dr_0 \\
&= -i \frac{k}{z_1} \exp\{i k z_1\} \exp\left\{i \frac{k}{2 z_1} r_1^2\right\} A_0 \int_0^\infty \exp\left\{i \frac{k}{2} \left(\frac{1}{z_1} - \frac{1}{f_0}\right) r_0^2\right\} \exp\left\{-\frac{r_0^2}{w_0^2}\right\} r_0 J_0\left\{\frac{k}{z_1} r_0 r_1\right\} dr_0.
\end{aligned} \tag{4-7}$$

The integral relationship $\int_0^\infty x \exp\{-\alpha x^2/2\} J_0(xy) dx = \frac{1}{\alpha} \exp\{-y^2/2\alpha\}$

can be applied to Eq. (4-7), where $x = r_0$, $y = k r_1/z_1$, and $\alpha = \frac{2}{w_0^2} - i k \left(\frac{1}{z_1} - \frac{1}{f_0}\right)$. The result is given in the following expression

$$\begin{aligned}
U_1(r_1) &= -i k w_0^2 \exp\{i k z_1\} \frac{2 z_1 + i k w_0^2 (1 - z_1/f_0)}{4 z_1^2 + k^2 w_0^4 (1 - z_1/f_0)^2} A_0 \\
&\times \exp\left\{-i \frac{k}{2 z_1} \left[\frac{k^2 w_0^4 (1 - z_1/f_0)}{4 z_1^2 + k^2 w_0^4 (1 - z_1/f_0)^2} - 1\right] r_1^2\right\} \exp\left\{-\frac{k^2 w_0^2 r_1^2}{4 z_1^2 + k^2 w_0^4 (1 - z_1/f_0)^2}\right\}.
\end{aligned} \tag{4-8}$$

This field description has the same structure as the original beam, in that both the amplitude and phase profiles are Gaussian. The beam radius at range z_l is

$$w_l = \sqrt{\frac{4 z_l^2 + k^2 w_0^4 (1 - z_l/f_0)^2}{k^2 w_0^2}}, \tag{4-9}$$

where the first term is the diffractive beam-spreading factor and the second describes the beam dimensions for geometrical propagation. The wavefront is defined by the focal distance

$$f_l = z_l \left[\frac{k^2 w_0^4 (1 - z_l/f_0)}{4 z_l^2 + k^2 w_0^4 (1 - z_l/f_0)^2} - 1 \right]^{-1}. \tag{4-10}$$

Note that the beam radius at range z_l is minimized when $f_0 = z_l$.

It will be useful to define a range parameter that specifies the onset of beam diffraction. According to Eq. (4-9), the beam radius will increase by a factor of $\sqrt{2}$ when the propagation range is

$$z_R = \frac{k w_0^2}{2} \left[1 + \frac{k w_0^2}{2 f_0} \right]^{-1} . \quad (4-11)$$

To compare this result with derivations developed for uniformly-illuminated apertures of diameter, D , it is useful to establish a relationship between D and w_0 . When the Airy irradiance pattern derived from the Fourier transformation of a circular aperture is compared with the far-field profile of a diffraction-limited Gaussian beam, the main-lobe structures are found to be closely matched when

$$D = 2^{3/2} w_0 . \quad (4-12)$$

Therefore, for a uniformly illuminated circular aperture

$$z_R = \frac{\pi D^2}{2^3 \lambda} \left[1 + \frac{\pi D^2}{2^3 \lambda f_0} \right]^{-1} . \quad (4-13)$$

For $f_0 = \infty$ this result closely approximates the standard definition, $z_R = D^2/\lambda$.

Well beyond the Rayleigh range the beam assumes the characteristics of a spherical wave originating from a point-source transmitter, as illustrated earlier in Figure 4-1. In the near field, where $z_1 \ll z_R$, the approximate expressions for w_1 , f_1 , and the multiplicative constant, A_1 , are

$$w_1 \approx w_0 \left(1 - z_1/f_0 \right) , \quad f_1 \approx f_0 - z_1 , \quad \text{and} \quad A_1 \approx \frac{A_0}{\left(1 - z_1/f_0 \right)} , \quad (4-14)$$

whereas in the far field of the transmitter

$$w_1 \approx \frac{2 z_1}{k w_0} , \quad f_1 \approx -z_1 , \quad \text{and} \quad A_1 \approx \frac{k w_0^2 A_0}{2 z_1} . \quad (4-15)$$

Once the far-field range limit has been reached, the beam radius and wavefront focus both scale linearly with propagation distance.

4.2 RECEIVER-PLANE FIELD EFFECTS DUE TO NEAR-FIELD PHASE PERTURBATIONS

For a few propagation geometries, such as vertical link between a large ground-based telescope and a high-altitude satellite, the accumulated channel distortions all effectively lie in the plane of the transmitter. In this case, the phase errors for a single realization can be added linearly and treated as a single distortion screen defined by the function, $\phi(x_0, y_0)$. The transmitter-plane representation of a perturbed Gaussian beam focused on a receiver at range $z = L$ is

$$\tilde{U}_0(x_0, y_0) = A_0 \exp\{i\phi(x_0, y_0)\} \exp\left\{-ik(x_0^2 + y_0^2)/2L\right\} \exp\left\{-(x_0^2 + y_0^2)/w_0^2\right\}. \quad (4-16)$$

The inclusion of the focus term places the receiver in the Fourier transform plane of the transmitter, in which case the Fraunhofer approximation can be applied to obtain the field at range L

$$\begin{aligned} \tilde{U}_L(x_L, y_L) &= \frac{k A_0}{2\pi L} \exp\left\{ik(x_L^2 + y_L^2)/2L\right\} \\ &\times \int_{-\infty}^{\infty} \int_{-\infty}^{\infty} \exp\{i\phi(x_0, y_0)\} \exp\left\{-(x_0^2 + y_0^2)/w_0^2\right\} \exp\left\{ik \frac{(x_0 x_L + y_0 y_L)}{L}\right\} dx_0 dy_0. \end{aligned} \quad (4-17)$$

(Complex constants having unity amplitude have been eliminated from this expression to simplify the notation.) With the variable substitutions, $\alpha = k x_0/L$ and $\beta = k y_0/L$, the previous equation can be written in the form of a Fourier transform

$$\begin{aligned} \tilde{U}_L(x_L, y_L) &= \frac{k A_0}{2\pi L} \exp\left\{ik(x_L^2 + y_L^2)/2L\right\} \\ &\times \mathcal{F}\left\{\exp\{i\phi(L\alpha/k, L\beta/k)\} \exp\left\{-(L^2\alpha^2 + L^2\beta^2)/k^2 w_0^2\right\}\right\}. \end{aligned} \quad (4-18)$$

which explicitly shows the range and wavelength dependence of the radial scaling. Note that the leading phase term is equivalent to that for a point source located in the plane of the transmitter, and in the absence of phase errors the second term is a simple Gaussian amplitude profile as described previously in Eq. (4-8). It should also be emphasized that since the outgoing wavefront has been tailored to optimize received power, all phase distortions inserted in the near-field result in a degradation of the far-field signal.

Recall that this derivation is based on the assumption that all channel effects are confined to the plane of the transmitter. This constraint can be relaxed somewhat by allowing the field perturbations to be placed further downrange, but within the Rayleigh-range limit. If the screen is located at range, z , with respect to the transmission aperture, then

$$\begin{aligned} \tilde{U}_L(x_L, y_L) = & \frac{k A_0}{2\pi L} \exp\left\{i k \left(x_L^2 + y_L^2\right) / 2L\right\} \\ & \times \mathcal{F}\left\{\exp\left\{i \phi(\gamma L \alpha / k, \gamma L \beta / k)\right\} \exp\left\{-\left(L^2 \alpha^2 + L^2 \beta^2\right) / k^2 w_0^2\right\}\right\}, \end{aligned} \quad (4-19)$$

where γ represents the radial scaling relationship between the unperturbed beam at the transmitter and the unperturbed beam at range z . Thus, from Eq. (4-9)

$$\gamma = \frac{w(z)}{w_0} = \sqrt{\left(1 - \frac{z}{L}\right)^2 + \frac{4 z^2}{k^2 w_0^4}}. \quad (4-20)$$

Since the beam is focused on the receiver, it initially shrinks in dimension but increases in size as the Rayleigh range is approached. The assumptions of the near-field approximation are clearly invalid when diffraction effects start to dominate and γ becomes significantly larger than 1. On the other hand, one could treat the previous expression as the sum of a geometrical-propagation component, which describes a beam that is focused to a point at the receiver and a spherical-wave component that emanates from the transmitter. The first of these two terms yields

$$\gamma \approx 1 - \frac{z}{L}, \quad (4-21)$$

which has appeared in a number of prior publications in which scintillation effects for focused-beam geometries have been investigated [8]. An accurate treatment of the spherical-wave component appears to require a very different set of assumptions and approximations, as described in the following section.

4.3 RECEIVER-PLANE FIELD EFFECTS DUE TO FAR-FIELD PHASE PERTURBATIONS

When the diameter of the transmitter becomes small enough to push most of the channel effects beyond the Rayleigh range, the propagation geometry begins to approach the point-source limit. In this case the perturbation and receiver planes cannot be treated as a Fourier conjugate pair, and their relationship must instead be defined through the Fresnel transformation. In general, signal fluctuations due to far-field perturbations are less severe since the relative separation between the two planes is smaller. A second important difference between the near-field and far-field geometries is that in the latter case the insertion of a phase screen will result in localized regions of signal enhancement due to focus contributions that counteract diffractive wavefront expansion (see Figure 4-2); when the channel effects are sufficiently weak, the mean irradiance will be identical to the diffraction-limited value. Both of these factors make it easier to apply Rytov analysis to far-field distortions.

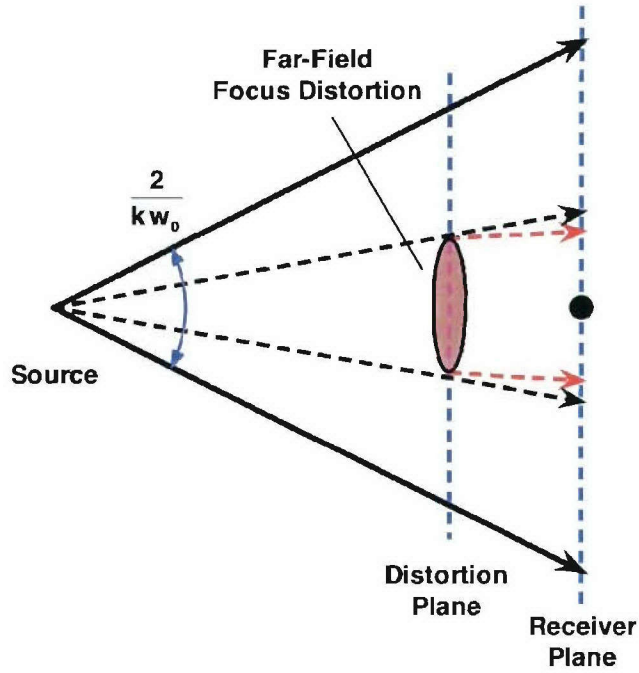


Figure 4-2. Illustration of the effect of placing a focusing element in the far-field of a point source. A point along the propagation axis will experience an increase or decrease in the optical irradiance, depending on the sign of the focusing element. Note that phase distortions that result in an on-axis irradiance enhancement only occur in the far field of the transmitter.

A mathematical description of Fraunhofer propagation from a source at $z=0$, through an intermediate plane at z_1 , and then to a second optical plane at z_2 was provided in Section 4.1. To simplify the notation and maintain consistency with the previous discussion, in this section the receiver's range will be represented as L , and the range to the intermediate perturbation plane will be given as z .

If the assumption is made that $z \gg z_R$, a Gaussian beam that encounters the perturbation field, ϕ , can be described as follows

$$\tilde{U}(x, y) = A \exp\{i\phi(x, y)\} \exp\left\{ik\left(x^2 + y^2\right)/2z\right\} \exp\left\{-\left(x^2 + y^2\right)/w^2\right\}, \quad (4-22)$$

and as specified in Eq. (4-15) $w \approx \frac{2z}{k w_0}$, and $A \approx \frac{k w_0^2 A_0}{2z}$. (4-23)

Fresnel propagation to L yields

$$\tilde{U}_L(x_L, y_L) = \frac{k}{2\pi(L-z)} \int_{-\infty}^{\infty} \int_{-\infty}^{\infty} \exp\left\{ik \frac{(x_L - x)^2 + (y_L - y)^2}{2(L-z)}\right\} U(x, y) dx dy . \quad (4-24)$$

This expression can be rearranged to incorporate the focus term in the Fresnel kernel, so that

$$\begin{aligned} \tilde{U}_L(x_L, y_L) &= \frac{k}{2\pi(L-z)} \exp\left\{ik(x_L^2 + y_L^2)/2L\right\} \\ &\times \int_{-\infty}^{\infty} \int_{-\infty}^{\infty} \exp\left\{ik \frac{L}{z} \frac{(zx_L/L - x)^2 + (zy_L/L - y)^2}{2(L-z)}\right\} U'(x, y) dx dy \end{aligned} \quad (4-25)$$

$$\text{where } U'(x, y) = A \exp\{i\phi(x, y)\} \exp\left\{-\frac{(x^2 + y^2)}{w^2}\right\} \quad (4-26)$$

is the product of the Gaussian amplitude and the perturbation field at z . The field transfer function can be expressed as

$$h'(x, y; x_L, y_L) \approx \frac{k}{2\pi(L-z)} \exp\left\{\frac{ik(x_L^2 + y_L^2)}{2L}\right\} \exp\left\{ik \frac{L}{z} \frac{(zx_L/L - x)^2 + (zy_L/L - y)^2}{2(L-z)}\right\} . \quad (4-27)$$

In the limit that the propagation distance $L - z$ is small compared to kw^2 , the third term of the previous expression can be replaced by a pair of delta functions by applying the identity

$$\delta(x) \equiv \lim_{a \rightarrow 0} \exp(-ax^2) / \sqrt{\pi/a} ,$$

thus yielding the result

$$h'(x, y; x_L, y_L) \approx \frac{z}{L} \exp\left\{\frac{ik(x_L^2 + y_L^2)}{2L}\right\} \delta\left(\frac{z}{L}x_L - x\right) \delta\left(\frac{z}{L}y_L - y\right) . \quad (4-28)$$

To first order, the field at L is simply a replica of U , which has been scaled along the radial axes by the factor L/z

$$\tilde{U}_L(x_L, y_L) \approx \frac{z}{L} \exp\left\{i k (x_L^2 + y_L^2) / 2 L\right\} U'\left(\frac{z}{L} x_L, \frac{z}{L} y_L\right) . \quad (4-29)$$

This solution represents the trivial case, where the beam propagation distance beyond the phase screen is too short to substantially modify the receiver-plane irradiance profile.

As the separation distance between z and L increases, the delta functions that appear in the previous expression must be replaced with a more accurate approximation. As illustrated in Figure 4-3, the integrals of both $\sin(ax^2)$ and $\cos(ax^2)$ display an abrupt, and approximately linear, transition centered at $x = 0$. The derivatives of both functions can therefore be replaced by the rectangle function, $\Pi(\sqrt{2a/\pi} x)$, where the normalization is given by the integral

$$\int_{-\infty}^{\infty} \int_{-\infty}^{\infty} \exp\left\{i a (x^2 + y^2)\right\} dx dy = i \frac{\pi}{a} .$$

The rectangle function establishes the linear dimensions of a characteristic integration region

$$\ell = \sqrt{\frac{2 \pi z (L - z)}{k L}} . \quad (4-30)$$

This results in the replacement of the delta functions with a two-dimensional average of $U'(x, y)$ centered at the point $\{z x_L / L, z y_L / L\}$, i.e.,

$$\begin{aligned} \tilde{U}_L(x_L, y_L) &\approx A \frac{z}{L} \exp\left\{i k (x_L^2 + y_L^2) / 2 L\right\} \\ &\times \frac{1}{\ell^2} \int_{-\ell/2}^{\ell/2} \int_{-\ell/2}^{\ell/2} \exp\left\{i \phi\left(\frac{z}{L} x_L - x, \frac{z}{L} y_L - y\right)\right\} \exp\left\{-\frac{1}{w^2} \left[\left(\frac{z}{L} x_L - x\right)^2 + \left(\frac{z}{L} y_L - y\right)^2\right]\right\} dx dy . \end{aligned} \quad (4-31)$$

At the nominal boresight location, the expression is further simplified

$$\tilde{U}_L(0, 0) \approx \frac{A z}{\ell^2 L} \int_{-\ell/2}^{\ell/2} \int_{-\ell/2}^{\ell/2} \exp\{i \phi(x, y)\} \exp\left\{-\left(x^2 + y^2\right) / w^2\right\} dx dy , \quad (4-32)$$

and if it is assumed that the physical dimensions of the beam at z are much larger than ℓ

$$\tilde{U}_L(0,0) \approx \frac{Az}{\ell^2 L} \int_{-\ell/2}^{\ell/2} \int_{-\ell/2}^{\ell/2} \exp\{i\phi(x,y)\} dx dy . \quad (4-33)$$

For the statistical analysis developed in the next section, it will be convenient to replace ℓ with the circular diameter

$$d_\ell = \sqrt{\frac{4}{\pi}} \ell = \sqrt{\frac{8 z_1 (z_2 - z_1)}{k z_2}} ,$$

or equivalently the Gaussian radius

$$w_\ell = 2^{-3/2} d_\ell = \sqrt{\frac{z_1 (z_2 - z_1)}{k z_2}} . \quad (4-34)$$

The physical interpretation of this result is that the scintillation experienced by a point in the receiver plane is only sensitive to far-field channel distortions that lie along the propagation axis and are within a radius defined by w_ℓ . However, as the range to the perturbation plane approaches the near-field region, this simple analytical description must be modified to account for plane-wave beam propagation within the transmitter radius, w_0 . As discussed below, these factors significantly reduce the impact of near-field phase fluctuations on the far-field contribution to the net scintillation.

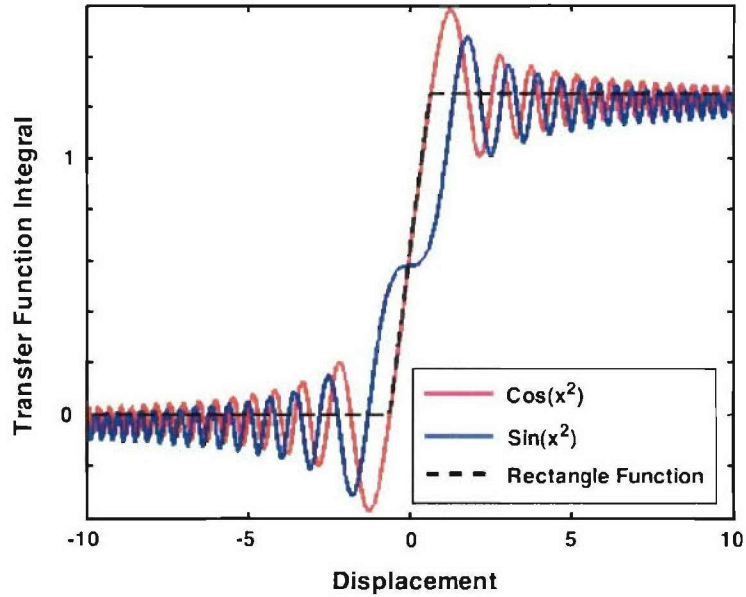


Figure 4-3. Comparison of the integrals of $\cos(x^2)$ and $\sin(x^2)$ with the integral of the rectangle function.

4.4 NUMERICAL SIMULATION TOOLS

The discussion of scintillation statistics provided in the next section derives from the analytical analysis presented earlier in this section, but is also heavily dependent on the results of numerical simulations of beamwave propagation performed at Lincoln Laboratory. The current version of the code, known as POPS, is a descendent of the three-dimensional time-dependent program, MOLLY, which was written at Lincoln Laboratory in the late 1980's to study turbulence and thermal blooming effects. Both programs incorporate subroutines to generate random Kolmogorov phase screens [14] and a means to propagate from one screen to the next using a two-dimensional Fresnel transformation [12]. As the beam propagates from screen to screen, the Talanov scale transformation [15] is imposed to maintain a constant ratio between the beam size and the dimensions of the field discretization grid. An arbitrary number of phase screens can be created to simulate the desired C_n^2 profile, and each screen can be moved perpendicular to the beam in accordance with the wind velocity profile for time-dependent simulations. Statistical behavior is typically characterized by running 100,000 independent realizations of the propagation channel. POPS is a state-of-the-art C-based code with a web-browser interface, which currently functions on a 16-node Xeon processor cluster.

For statistical investigations, the output of the POPS code is generally configured to record the irradiance at a small number of grid points within the receiver plane. However, to obtain a better understanding of the physical processes that drive beam scintillation, it is often useful to study selected images of the entire profile. The evolution of the dominant phenomenological mechanisms that drive far-field scintillation are clearly illustrated by the beam images shown in the next section. In support of this investigation, an extensive set of simulations have been performed for the vertical propagation geometry to a receiver at 40 Mm and horizontal propagation to a receiver at 10 km. The tilt-removed results that are described in the next section were obtained by measuring the irradiance for each realization at the grid point located at the center of mass of the far-field beam profile.

5. IRRADIANCE STATISTICS AT THE RECEIVER-PLANE BORESIGHT

In this section separate scintillation index expressions will be developed for each of the three beam-propagation regimes defined previously; specifically, $w_0/r_0 \ll 1$, $w_0/r_0 \approx 1$, and $w_0/r_0 \gg 1$. It is only in the first of these cases, where the geometry approaches the point-source limit, that far-field channel effects tend to dominate scintillation behavior.

The parameter terminology introduced in the previous section will be continued in this discussion, including the use of the Gaussian beam radius w_0 to characterize the dimensions of the transmitted beam. This analysis begins with the case that is best characterized by traditional statistical descriptions based on the Rytov approximation.

5.1 SCINTILLATION INDEX FOR $w_0/r_0 \ll 1$: WEAK FAR-FIELD TURBULENCE

The propagation relationships developed in Section 4.3 demonstrate that when the transmitted beam diameter is very small, the phase perturbation and the receiver planes both lie in the far field of the transmitter. In this limit, the detected irradiance fluctuations due to a perturbation field at range z are only influenced by an illuminated region of radius

$$w_\ell \approx \sqrt{\frac{z(L-z)}{kL}}, \quad (5-1)$$

which is generally much smaller than the physical dimensions of the diffraction-limited beam. To first order, the net impact of phase distortions within this region can be modeled as a thin lens that either enhances or counteracts diffractive beam spreading. At the receiver plane, this effect produces a weak multiplicative modulation of the diffraction-limited beam profile, as quantified earlier in Eq. (4-33).

The beam image and profile examples given in Figure 5-1 show little evidence of either pointing jitter or time-averaged shape distortions. The primary feature illustrated in these pictures is a high spatial-frequency speckle pattern that imposes relatively shallow fades. In this environment, the assumptions associated with the Rytov approximation are valid, and numerical simulations show that the on-axis irradiance distribution is approximately log-normal with a mean Strehl that is close to unity.

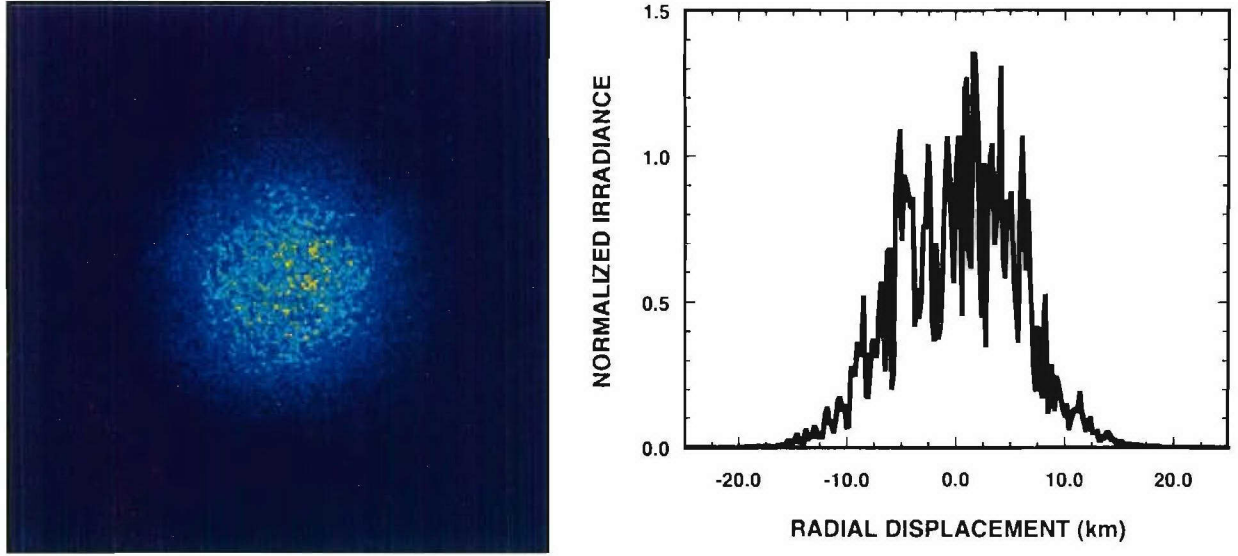


Figure 5-1. Far-field beam image (left figure) and horizontal-axis profile (right figure) for $w_0/r_0 = 0.01$. The Hufnagel-Valley turbulence profile was used in this simulation of vertical propagation, which resulted in an r_0 value of 19 cm at 1.55 mm. The propagation distance is 40 Mm, and the linear dimension of the image fields is 50 km. The long-exposure beam profile is approximately diffraction-limited.

Estimates of the scintillation index for the point-source limit follow directly from the work of a number of investigators in the field of adaptive optics [16]. Following Sasiela's derivation [8], the focused-beam scintillation index for Kolmogorov turbulence would be expressed as follows

$$\sigma_I^2 = 0.829 k^2 \int_0^L C_n^2(z) \int \kappa^{-1/3} \sin^2 \left[\frac{\kappa^2 z (L-z)}{2 k L} \right] d\vec{\kappa} dz, \quad (5-2)$$

where $\vec{\kappa}$ is the spatial frequency vector. The $\sin^2[\bullet]$ term that appears in this expression represents the filter function for a spherical aperture, which captures the effect of the far-field integration region, w_t , defined in Eq. (5-1). For a point source, the evaluation of the integral over the κ vector gives

$$\sigma_I^2 = 2.25 k^{7/6} \int_0^L C_n^2(z) z^{5/6} \left(\frac{L-z}{L} \right)^{5/6} dz. \quad (5-3)$$

Several authors define the propagation parameter, $\gamma = z/L$, and express this equation as follows

$$\sigma_I^2 = 2.25 k^{7/6} \int_0^L C_n^2(z) (L-z)^{5/6} \gamma^{5/6} dz \quad (5-4)$$

The previous result can be extended to include transmitters of finite dimension by appropriately modifying the argument of the integral in Eq. (5-2). The approach employed here is similar to that developed by Sasiela to evaluate the magnitude of scintillation for extended sources and receivers. The effects of an extended source of radius, w_s , situated at range z are described by the filter function

$$F(\kappa) = \left[\frac{2 J_1(\sqrt{2} \kappa w_s)}{\sqrt{2} \kappa w_s} \right]^2 \quad (5-5)$$

so that Eq. (5-2) can be rewritten as

$$\sigma_I^2 = 0.829 k^2 \int_0^L C_n^2(z) \int \kappa^{-1/3} \sin^2 \left[\frac{\kappa^2 z (L-z)}{2 k L} \right] \left[\frac{2 J_1(\sqrt{2} \kappa w_s)}{\sqrt{2} \kappa w_s} \right]^2 d\bar{\kappa} dz \quad (5-6)$$

When the ratio, $k w_s^2 / z$, is large, the integration over κ can be approximated by

$$\sigma_I^2 \approx 1.53 \int_0^L C_n^2(z) z^2 \left(\frac{L}{L-z} \right)^{1/3} w_s^{-7/3} dz \quad (5-7)$$

The transition between Eqs. (5-3) and (5-7) can be accomplished by postulating a range-dependent source radius of the form

$$w_s = w_0 \sqrt{1 + 0.719 \frac{L}{(L-z)} \frac{z}{k w_0^2}} \quad (5-8)$$

which is proportional to \sqrt{z} beyond the Rayleigh range. The final result can be expressed in the form of Eq. (5-4), but with the following modification of the propagation parameter

$$\gamma = \left(\frac{z}{L} \right) \left[1 + 1.39 \left(\frac{L-z}{L} \right) \frac{k w_0^2}{z} \right]^{-7/5} \quad (5-9)$$

Note that with this version of the γ parameter, the scintillation index approaches zero monotonically as w_0 becomes large. It must be emphasized, however, that this prediction assumes that all perturbation

effects are confined to the far-field region of the transmitter. This relationship is similar to an expression derived by Sasiela for beamwave propagation [8]. An alternative derivation of the scintillation index for this case is given in the Appendix.

For future studies of time-dependent behavior it is perhaps of interest to briefly address the characteristic feature dimensions of the speckle pattern illustrated in Figure 5-1. An examination of sample profiles for a range of w_0 values reveals that the speckle dimensions are relatively insensitive to the size of the transmitted beam, so that the number of speckles within the diffraction-limited far-field profile is inversely proportional to w_0^2 . This result is supported by a calculation of the coherence diameter measured in the plane of the receiver for small-beam illumination. Using the definition for γ given above, the characteristic angular dimension of the speckle features is predicted to be

$$\theta_s \equiv \frac{r_0}{L} = \left[0.423 k^2 \int_0^L C_n^2(z) z^{5/3} \left(1 + 1.39 \left(\frac{L-z}{L} \right) \frac{k w_0^2}{z} \right)^{-7/3} dz \right]^{-3/5}. \quad (5-10)$$

For small values of w_0 this result is independent of the transmitted beam diameter, and the estimates derived from this expression are found to be in good agreement with profile realizations obtained from numerical simulations.

Figure 5-2 shows a plot of scintillation index values derived from the POPS code for an uplink geometry through a Hufnagel-Valley turbulence profile and horizontal-path propagation over a 10 km path for $C_n^2 = 1.39 \times 10^{-16} \text{ m}^{-2/3}$. In both cases, the r_0 value was computed for focused-beam propagation from 0 to L , as described in Eq. (3-1)

$$r_0 = \left[0.423 k^2 \int_0^L C_n^2(z) \left(\frac{L-z}{z} \right)^{5/3} dz \right]^{-3/5}.$$

The dashed lines included in this figure indicate the scintillation index predicted for the small w_0/r_0 limit using the propagation parameter expression given in Eq. (5-9). The model accurately describes the data until w_0/r_0 approaches unity.

All of the results presented in this section are consistent with traditional analyses based on the first-order Rytov approximation. In the next two sections, it will be shown that alternative methodologies are required when w_0/r_0 becomes large.

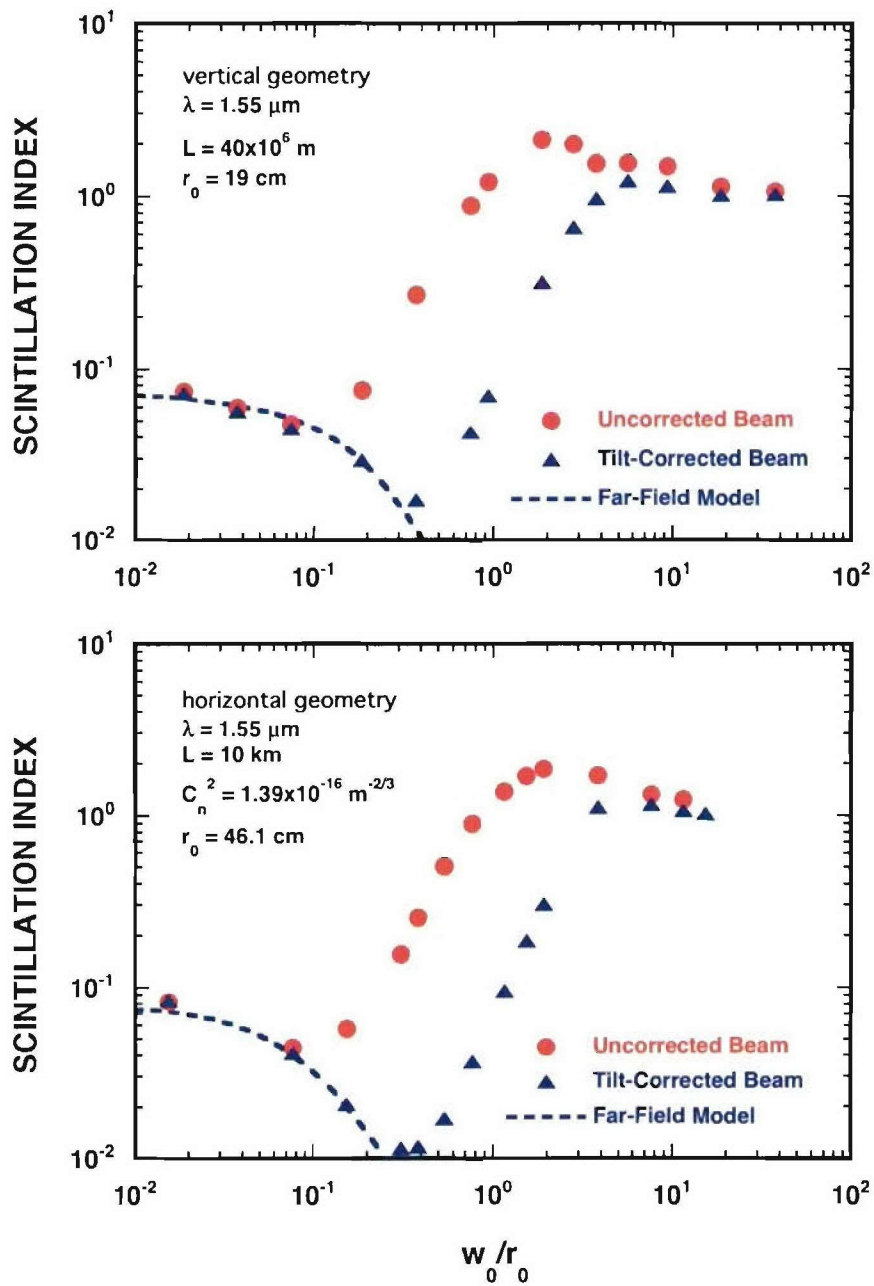


Figure 5-2. Comparison of simulation results (red and blue data points) with the model for turbulence concentrated in the far-field of the transmitter (blue dashed line). The upper figure represents an uplink geometry and the lower is horizontal propagation to 10 km.

5.2 SCINTILLATION INDEX FOR $w_0/r_0 \approx 1$: MODERATE NEAR-FIELD TURBULENCE

In many respects, the moderate turbulence case is the most interesting and least understood of the three scenarios treated in this report. Numerical simulations performed at Lincoln Laboratory show significant discrepancies between measured statistical behavior and the predictions based on log-normal models. A distinguishing characteristic of the irradiance distributions derived from large ensembles of independent channel realizations is an extended power-law tail in the low-signal region of the probability density function. The impact of this discrepancy is that the log-normal models grossly underestimate the likelihood of deep signal fades. Inspections of beam images at the receiver-plane disclose a consistent pattern; for moderate levels of uncorrected turbulence, beam jitter is the dominant effect.

The examples shown in Figure 5-3 provide some insight into the mechanisms that govern beam statistics when the w_0/r_0 ratio is of order unity. The far-field profile is generally characterized by a single main lobe that is somewhat larger than a diffraction-limited beam, which becomes more distorted as w_0/r_0 increases. In this regime, however, irradiance fluctuations at the receiver's boresight are driven primarily by beam motion if tilt correction is not implemented. Note that the small speckle features that were prominent in Figure 5-1 are not found in this image.

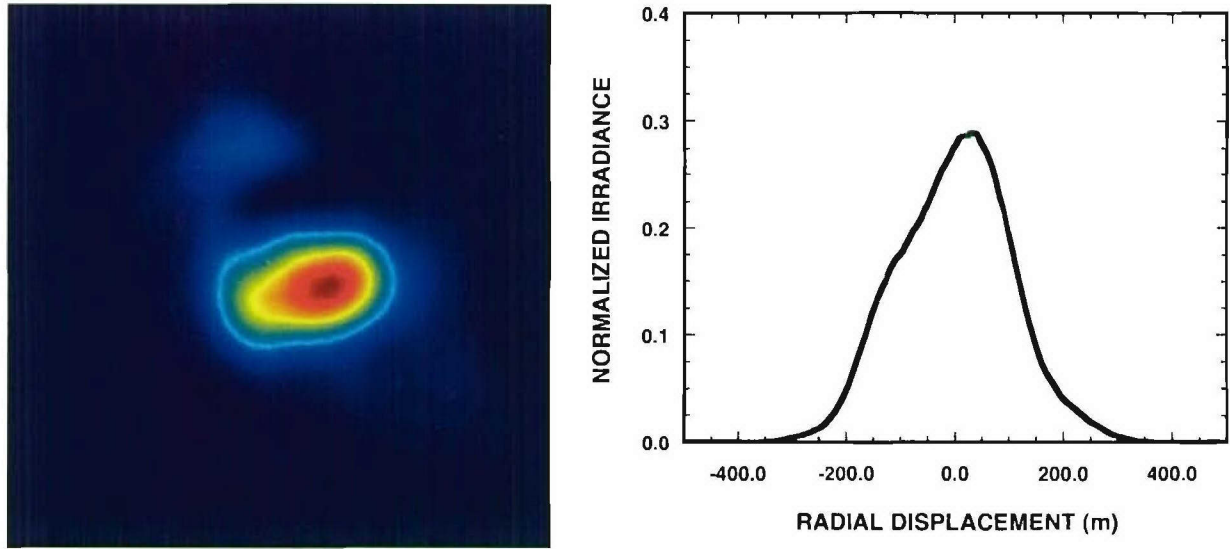


Figure 5-3. Far-field beam image (left figure) and horizontal-axis profile (right figure) for $w_0/r_0 = 1$. The Hufnagel-Valley turbulence profile was used in this simulation of vertical propagation, which resulted in an r_0 value of 19 cm at 1.55 μm . The propagation distance is 40 Mm, and the linear dimension of the image field is 1 km.

Within the adaptive-optics community, calculations of the far-field Strehl are usually derived from estimates of the accumulated phase errors over the entire propagation path. Since the engagement geometries typically involve targets that are well outside of the atmosphere, this approach is equivalent to collapsing all of the channel perturbations into a single phase screen within the near field of the transmitter. For Kolmogorov turbulence, Noll has shown that the phase variance due to atmospheric tilt jitter is nearly an order of magnitude larger than the combined contributions of the higher-order Zernike modes [11]. A scintillation analysis based solely on beam jitter provides significant insight into the underlying physical mechanisms that dominate receiver fluctuations when $w_0 \approx r_0$.

A rough estimate of fluctuation statistics due to turbulence-induced tilt can be made by assuming that the far-field beam profile and the tilt-jitter distribution are both described by Gaussian functions. Using ρ and θ to represent the radial and vectorial angles with respect to boresight, the normalized beam profile at range L can be written as

$$I(\rho) \approx \exp \left\{ -2 \left(\frac{\rho}{w_L/L} \right)^2 \right\}, \quad (5-12)$$

where w_L is the far-field beam radius; the distribution of the beam displacement angle would be

$$p_{\text{tilt}}(\rho) = \int_0^{2\pi} p_{\text{tilt}}(\rho, \theta) \rho d\theta = \frac{\rho}{\sigma_t^2} \exp \left\{ -\frac{\rho^2}{2\sigma_t^2} \right\}, \quad (5-13)$$

where σ_t is the single-axis jitter radius. The tilt distribution can be converted to an on-axis Strehl distribution by combining the last two expressions

$$p(S) \approx \begin{cases} m S^{m-1} & : 0 \leq S \leq 1 \\ 0 & : 1 < S \end{cases}, \quad (5-14)$$

where $m = \frac{(w_L/L)^2}{4\sigma_t^2}$. (5-15)

Similar relationships have been previously published by Fried and Titterton [17,18]. Simulation results for uncorrected turbulence support this model, as discussed in Section 6.

An estimate of the power-law parameter, m , is obtainable given knowledge of w_L and σ_I . The first parameter follows from Eq. (4-9)

$$w_L = \frac{2L}{k w_0} \quad (5-16)$$

and the second derives from a calculation of the Zernike tilt component of turbulence developed by Sasiela [8]

$$\sigma_I^2 = \frac{5.09}{k^2 r_0^{5/3} w_0^{1/3}} \quad (5-17)$$

which yields the result

$$m \approx 0.196 \left(\frac{w_0}{r_0} \right)^{-5/3} \quad (5-18)$$

The scintillation index obtains from the moments of Eq. (5-14)

$$\langle I^k \rangle = \int_0^1 I^k p(I) dI = \frac{m}{m+k} \quad (5-19)$$

so that

$$\sigma_I^2 \equiv \frac{\langle I^2 \rangle}{\langle I \rangle^2} - 1 = \frac{1}{m(m+2)} \quad (5-20)$$

Note that this predicts that m will be proportional to $(w_0/r_0)^{10/3}$ when the ratio is small and $(w_0/r_0)^{5/3}$ when it is large, which is in qualitative agreement with prior estimates [19,20].

Unfortunately, the analytical approach just described provides little guidance with regard to the scintillation properties of a tilt-corrected transmitter. For that case, one would expect that irradiance fluctuations will be primarily driven by the changing dimensions of the beam's main lobe and variations in the combined strength of the secondary lobes. On the other hand, Eq. (5-20) does suggest that the scintillation index should be roughly proportional to the transmitter-plane phase variance, which according to Noll's estimates are all proportional to the 5/3 power of the w_0/r_0 ratio [11]

$$\text{total phase variance: } \sigma_{\phi}^2 \approx 1.03 (D/r_0)^{5/3} = 5.83 (w_0/r_0)^{5/3} \quad (5-21)$$

$$\text{tilt-removed phase variance: } \sigma_{\phi}^2 \approx 0.134 (D/r_0)^{5/3} = 0.758 (w_0/r_0)^{5/3} . \quad (5-22)$$

Following this reasoning, one might expect the functional forms for the uncorrected and tilt-corrected scintillation index to be similar, but with leading constants that differ by about an order of magnitude.

In Figure 5-4, the scintillation index results from the POPS code that were introduced previously are compared with models of the form $\sigma_I^2 = a (w_0/r_0)^b$ within the transition region between the point-source and large-aperture limits. As before, the coherence diameter is computed for focused beam propagation from 0 to L , as defined in Eq. (3-1)

$$r_0 = \left[0.423 k^2 \int_0^L (1-z/L)^{5/3} C_n^2(z) dz \right]^{-3/5} : \text{focused beam} .$$

In the regime where near-field phase perturbation dominate the shape of the far-field beam, the scintillation index function displays a strong power-law behavior. A least-square fit to the uncorrected turbulence data yields the result

$$\sigma_I^2 \approx 1.30 (w_0/r_0)^{5/3} = 0.550 k^2 w_0^{5/3} \int_0^L (1-z/L)^{5/3} C_n^2(z) dz , \quad (5-23)$$

which is consistent with predictions based on Eq. (5-20). The shape of the tilt-removed scintillation index is similar, but a $7/3$ power-law exponent provides a better fit to the data than the $5/3$ exponent used in the last expression

$$\left[\sigma_I^2 \right]_{fig} \approx 0.078 (w_0/r_0)^{7/3} = 0.0234 k^{14/5} w_0^{7/3} \left[\int_0^L (1-z/L)^{5/3} C_n^2(z) dz \right]^{7/5} . \quad (5-24)$$

These results are judged to be highly significant, in that the same set of expressions have been successfully applied to both an uplink and a horizontal-path geometry for which the C_n^2 profile descriptions are very different. Additional simulation runs are planned to assess the range of applicability of these two relationships.

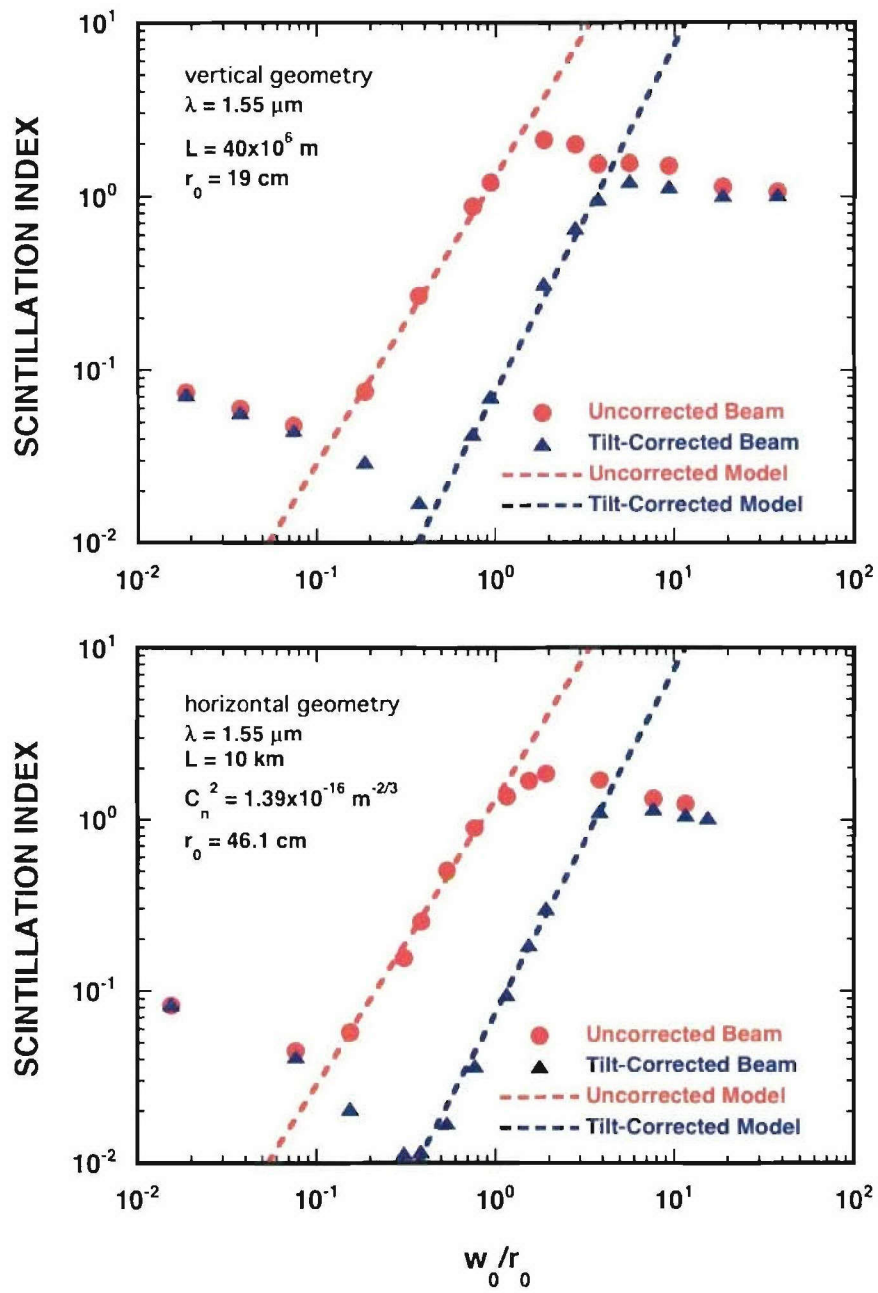


Figure 5-4. Comparison of simulation results (red and blue data points) with the transition-region scintillation models (dashed lines). The upper figure represents an uplink geometry and the lower is horizontal propagation to 10 km.

5.3 SCINTILLATION INDEX FOR $w_0/r_0 \gg 1$: SATURATION DUE TO STRONG NEAR-FIELD TURBULENCE

In the limit of far-field beam saturation, the irradiance profile is characterized by multiple lobes of roughly equal intensity separated by deep nulls. The angular dimensions of both the bright and dim regions are of the order of $1/k w_0$. Two representative images are shown in Figure 5-5.

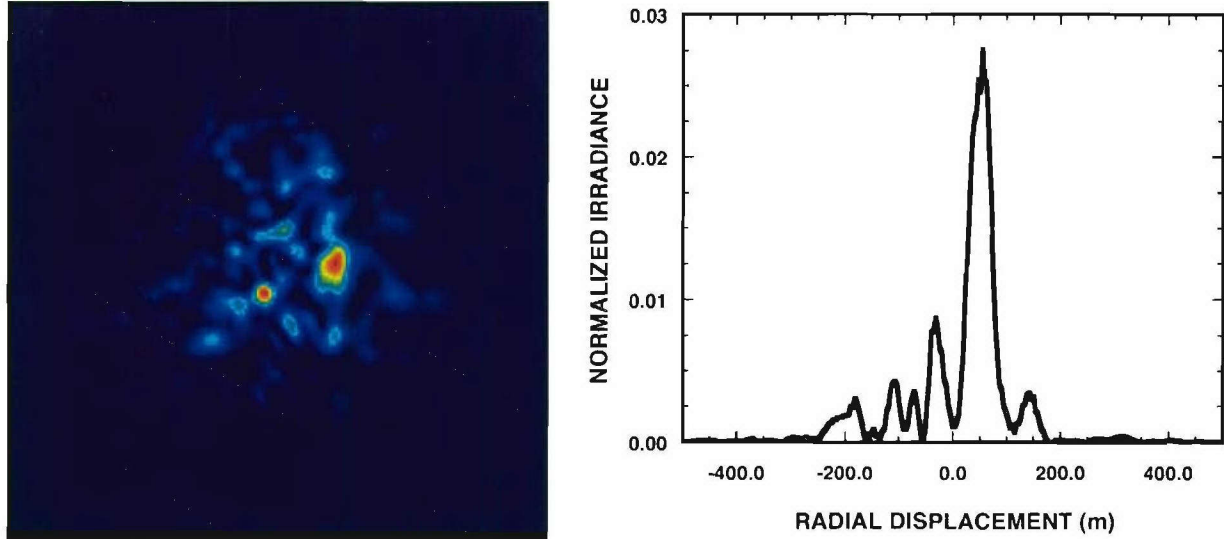


Figure 5-5. Far-field beam image (left figure) and horizontal-axis profile (right figure) for $w_0/r_0 = 5$. The Hufnagel-Valley turbulence profile was used in this simulation of vertical propagation, which resulted in an r_0 value of 19 cm at 1.55 mm. The propagation distance is 40 Mm, and the linear dimension of the image fields is 1 km. The average dimension of the individual speckles is approximately diffraction-limited.

Superficially, this picture bears a resemblance to the beam profile for the small-beam case shown in Figure 5-1, but the physical processes involved are very different. Recall that for the point-source limit, the long-exposure beam width is essentially diffraction-limited, and the superimposed modulation pattern is characterized by relatively shallow spatial features having an angular extent that is small compared to λ/w_0 . In the saturation limit, the size of the long-exposure profile is of the order of λ/r_0 , and each of the speckle features is essentially an independent diffraction-limited beam with random intensity and offset angle. Since the superposition of the ensemble of beams is coherent, the null regions between the peaks tend to be very deep.

Although the physical structure of this chaotic behavior seems very complex, the statistical descriptions of the fields in both the transmitter and receiver planes are surprisingly simple. An important result of the numerical simulations performed as part of this investigation is the discovery that far-field irradiance saturation is strongly correlated with saturation of phase errors in the near field of the transmitter. If the optical phase at each point in the transmitter plane is described by the residual, \mathcal{G} , within the range $\pm\pi$ such that $\phi = \mathcal{G} + n2\pi$, saturation occurs when the distribution of \mathcal{G} becomes uniform

$$p(\mathcal{G}) = \frac{1}{2\pi} : -\pi \leq \mathcal{G} \leq \pi . \quad (5-25)$$

This condition is clearly at odds with the Rytov approximation, which assumes that the magnitude of \mathcal{G} is small compared to π and that its distribution is Gaussian.

One way to model the far-field effects of the phase distribution given in the previous expression is to divide the transmitted beam into an ensemble of N uncorrelated sources. It is reasonable to expect that the characteristic spatial dimension of each source will be of the order of r_0 , so that $N \propto (w_0/r_0)^2$. If each discrete source is described by the phase, \mathcal{G}_i , in the Fourier transform plane, the on-axis Strehl is the phasor sum [21]

$$S = \left| \frac{1}{N} \sum_{i=1}^N \exp\{i\phi_i\} \right|^2 . \quad (5-26)$$

If the distribution of the random variable, \mathcal{G}_i , is uniform, the distribution of S is specified by the negative exponential function

$$p(S) = N \exp\{-N S\} , \quad (5-27)$$

which is confirmed by the numerical simulations. The first two moments of this model and the associated scintillation index are summarized in the following expressions:

$$\langle S \rangle = \frac{1}{N} , \quad \sigma_S^2 = \frac{1}{N^2} , \quad \text{and} \quad \sigma_I^2 \equiv \frac{\sigma_S^2}{\langle S \rangle^2} = 1 . \quad (5-28)$$

While this scintillation index derived from this model is not sensitive to the magnitude of N (as long as N is large), an estimate of this number is required to compute the mean Strehl ratio. The earlier prediction that $N \propto (w_0/r_0)^2$ is discussed in Section 5.5, which provides an overview of the Strehl models investigated in this study.

5.4 COMBINING THE SCINTILLATION INDEX MODELS

Arguments have been presented in this section to support the concept that beamwave scintillation can be divided into at least three distinct regions of behavior—the small-aperture geometry in which phase perturbations are concentrated in the far-field of the transmitter, the $w_0 \approx r_0$ scenario for which phase perturbations are concentrated in the near-field of the transmitter, and saturated scintillation due to strong perturbations in the near-field of the transmitter. The second case has been subdivided into uncorrected and tilt-corrected (figure) turbulence; the latter case being the more desirable configuration and the one more likely to be implemented in a practical system. Since beam-jitter correction is never perfect, these two examples provide upper and lower limits on system performance.

The scintillation index models that have been developed thus far can be summarized as follows:

far-field effects that are accurately modeled by the Rytov approximation.

$$\left[\sigma_I^2 \right]_{FF} \approx 2.25 k^{7/6} \int_0^L z^{5/6} (1-z/L)^{5/6} \left[1 + 1.39 (1-z/L) \frac{k w_0^2}{z} \right]^{-7/6} C_n^2(z) dz , \quad (5-29)$$

near-field effects driven by tilt and figure distortions:

$$\left[\sigma_I^2 \right]_{NF} = 0.550 k^2 w_0^{5/3} \int_0^L (1-z/L)^{5/3} C_n^2(z) dz \quad (5-30)$$

$$\left[\sigma_I^2 \right]_{NF,fig} = 0.0234 k^{14/5} w_0^{7/3} \left[\int_0^L (1-z/L)^{5/3} C_n^2(z) dz \right]^{7/5} , \quad (5-31)$$

and saturation due to near-field perturbations:

$$\left[\sigma_I^2 \right]_{SAT} = 1 . \quad (5-32)$$

The following heuristic expressions combine these relationships in such a way that a smooth transition between each of the regions is accomplished

$$\left[\sigma_I^2 \right] = \frac{\sqrt{\left[\sigma_I^2 \right]_{FF}^2 + \left[\sigma_I^2 \right]_{NF}^2}}{1 + \exp\{-3r_0/w_0\} \left[\sigma_I^2 \right]_{NF}} \quad (5-33)$$

$$\left[\sigma_I^2\right]_{fig} = \frac{\sqrt{\left[\sigma_I^2\right]_{FF}^2 + \left[\sigma_I^2\right]_{NF,fig}^2}}{1 + \exp\{-3r_0/w_0\} \left[\sigma_I^2\right]_{NF,fig}} . \quad (5-34)$$

Recall that r_0 is defined for the focused-beam geometry

$$r_0 = \left[0.423 k^2 \int_0^L (1-z/L)^{5/3} C_n^2(z) dz \right]^{-3/5} .$$

The exponential term in the denominators of Eqs. (5-33) and (5-34) introduces a small amount of overshoot at the initiation of saturation, which is consistently observed in the results of the numerical simulations.

It has been suggested by some authors that systems designed to operate near the minimum of the scintillation index curve provide optimal performance. Since channel conditions can be highly variable, this strategy may not be practical, but it is worth noting that this design point can be computed from the composite σ_I^2 expressions given above

$$\text{uncorrected turbulence minimum: } w_0^4 \approx 2.78 k^{-2} \frac{\int_0^L z^2 (1-z/L)^{-1/3} C_n^2(z) dz}{\int_0^L (1-z/L)^{5/3} C_n^2(z) dz} \quad (5-35)$$

$$\text{tilt-corrected turbulence minimum: } w_0^{14/3} \approx 65.4 k^{-14/5} \frac{\int_0^L z^2 (1-z/L)^{-1/3} C_n^2(z) dz}{\left[\int_0^L (1-z/L)^{5/3} C_n^2(z) dz \right]^{7/5}} . \quad (5-36)$$

A comparison of the composite scintillation index models derived in this section and simulation results obtained from Lincoln Laboratory's POPS code are shown in Figure 5-6. The agreement between the models and data is very good, and as noted before, the same pair of expressions has been applied to both the uplink and horizontal-path propagation geometries.

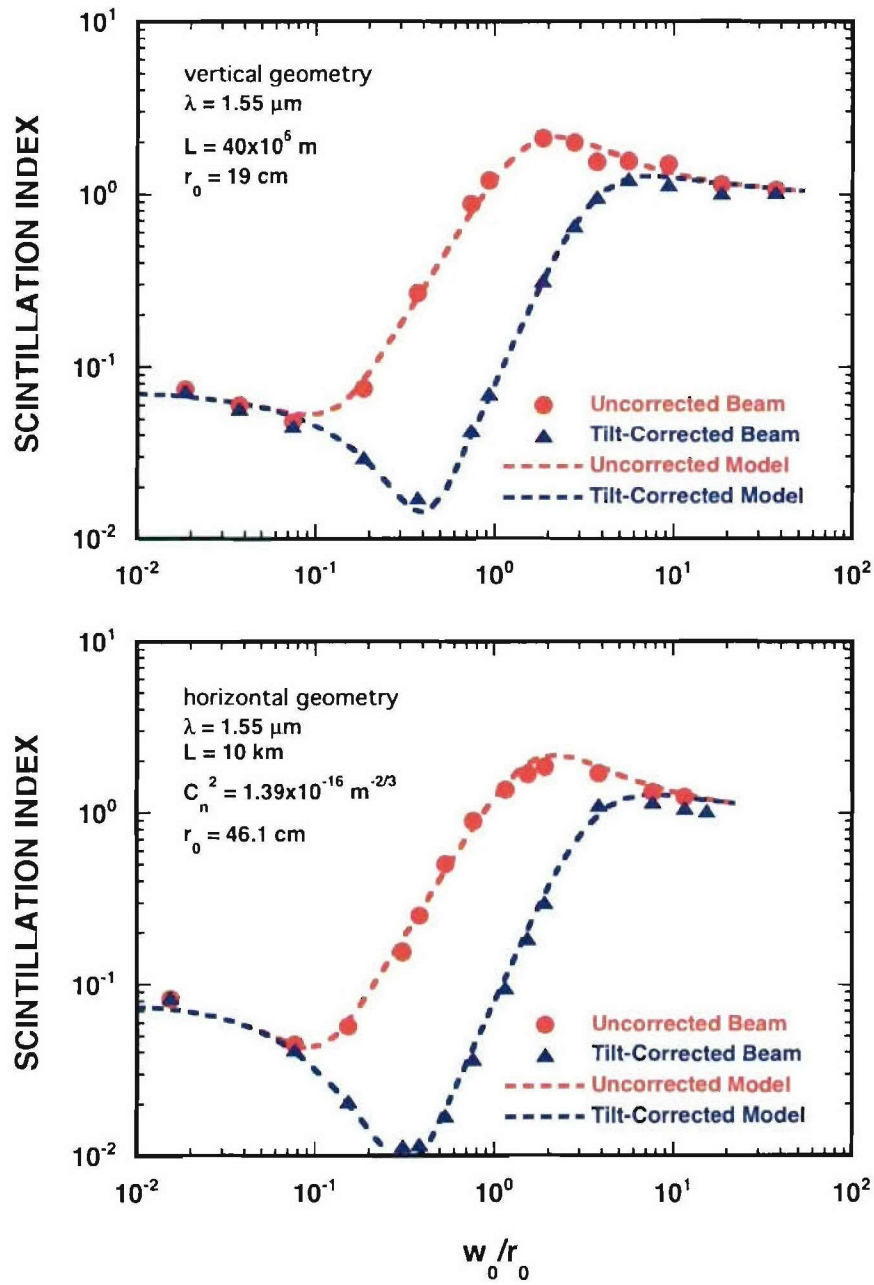


Figure 5-6. Comparison of simulation results (red and blue data points) with the composite scintillation index models (dashed lines). The upper figure represents an uplink geometry and the lower is horizontal propagation to 10 km.

5.5 STREHL RATIO MODELS

Investigations of scintillation often fail to include any discussion of the average Strehl ratio, which is surprising in that accurate knowledge of this quantity is essential for any system application where the optical source is limited by size, weight, or electrical power constraints. This section provides Strehl approximations for uncorrected and tilt-corrected turbulence; both relationships are shown to be highly reliable over a wide range of channel conditions.

The extended Maréchal approximation, which relates the Strehl to the transmitter-plane phase variance, is used extensively by the adaptive-optics community

$$\langle S \rangle \approx \exp \left\{ -\sigma_\phi^2 \right\} . \quad (5-37)$$

To estimate the value of σ_ϕ^2 , the Zernike-component estimates given in Eqs. (5-21) and (5-22) are typically referenced. While this approach is usually adequate when the phase variance is small, alternative representations have been developed that are accurate for a wider range of σ_ϕ^2 values. A notable example is one published by Andrews and Phillips [13]

$$\langle S \rangle \approx \left[1 + 5.56 (w_0/r_0)^{5/3} \right]^{-6/5} . \quad (5-38)$$

A number of authors, including Yura [7], have drawn a distinction between the short-exposure tilt-included and short-exposure tilt-removed turbulence coherence diameter. An understanding of this distinction is very important for systems that incorporate high-bandwidth closed-loop beam tracking. In the scintillation index plots shown earlier, it was demonstrated that tilt effects become a dominant concern when w_0/r_0 is of order unity. It is not surprising, therefore, that differences between the uncorrected and tilt-corrected Strehl ratios would become significant in this region. The following relationship, which is a modified version of Eq. (5-38), eliminates the tilt component of the Zernike phase variance until saturation is achieved

$$\langle S \rangle_{fig} \approx \left[1 + \left(5.56 - \frac{4.84}{1 + 0.04 (w_0/r_0)^{5/3}} \right) (w_0/r_0)^{5/3} \right]^{-6/5} . \quad (5-39)$$

Comparisons of these models with results obtained from the POPS code are shown in Figure 5-7. These last two relationships, in conjunction with the expressions for the scintillation index given previously in Eqs. (5-33) and (5-34), provide a highly accurate means of estimating the low-order statistical moments of the receiver-plane irradiance for a wide range of propagation conditions.

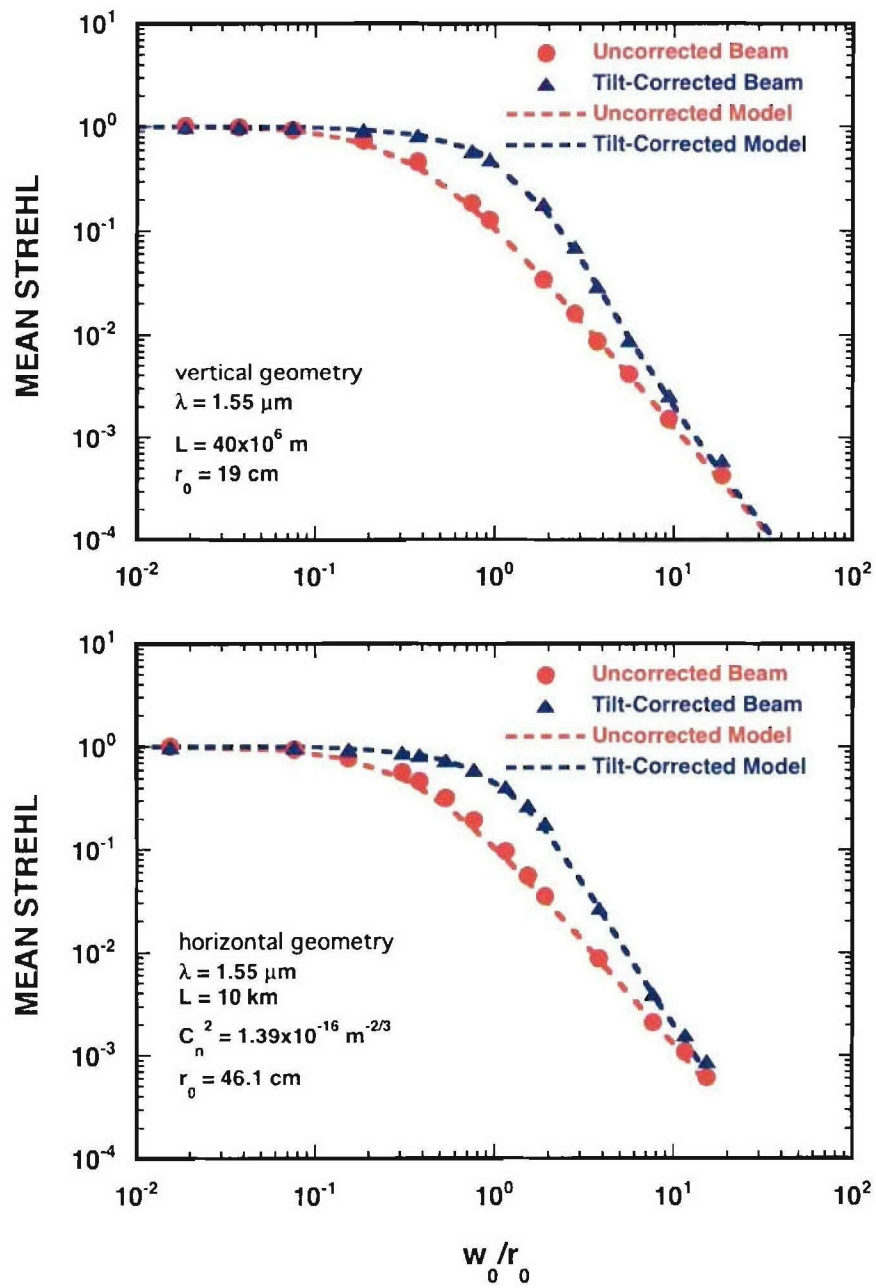


Figure 5-7. Comparison of simulation results (red and blue data points) with the Strehl ratio models (dashed lines). The upper figure represents an uplink geometry and the lower is horizontal propagation to 10 km.

6. RECEIVER-PLANE IRRADIANCE DISTRIBUTION MODELS

For many system constructs, the estimates of the mean Strehl and scintillation index developed in the last section are adequate to provide a first-order estimate system performance. However, some applications, including free-space optical communications, require a more detailed knowledge of the irradiance statistics at the plane of the receiver. In this section, distribution models are developed for the three sets of conditions discussed earlier, i.e., $w_0/r_0 \ll 1$, $w_0/r_0 \approx 1$, and $w_0/r_0 \gg 1$. The complexity of the mathematics parallels that of the last section in that the models for the large and small aperture limits have relatively simple descriptions, whereas the intermediate case is much more difficult to accurately represent.

A successful scintillation model must satisfy several constraints, in addition to the obvious requirement for accuracy. Mathematical simplicity is a primary concern, since the distribution function is likely to become a building block in a high-level model of overall system performance. It is also important to be able to associate the free parameters of the model with measurable properties of the channel, such as the C_n^2 profile. Statistical models that lack these properties are of little use in engineering design studies.

Before proceeding, it should be noted that much of the literature relating to this subject assumes that log-normal distribution is appropriate for almost all propagation geometries. The work of Andrews et al. [22] is a rare example of an alternative statistical description that accurately describes scintillation for a wide range of propagation geometries. The three-parameter formulation proposed by Andrews is known as the gamma-gamma model, which can be described as the product of a power-law function and the K-Bessel function

$$p(S) = \frac{2(\alpha\beta)^{(\alpha+\beta)/2}}{\Gamma(\alpha)\Gamma(\beta)\langle S \rangle} \left(\frac{S}{\langle S \rangle} \right)^{(\alpha+\beta)/2-1} K_{\alpha-\beta} \left\{ 2\sqrt{\alpha\beta S/\langle S \rangle} \right\} . \quad (6-1)$$

The α and β parameters can be related to the strength of large- and small-scale phase perturbations, respectively. Although the models developed in this section have a somewhat different structure, they share many of the essential properties of the gamma-gamma function.

6.1 DISTRIBUTION MODEL FOR $w_0/r_0 \ll 1$: WEAK FAR-FIELD TURBULENCE

Recall from Section 2 that the Rytov approximation assumes a multiplicative field perturbation of the form

$$U_\varepsilon = \exp\{\chi + i\phi\} , \quad (6-2)$$

which indicates that irradiance fluctuations derive from the real part of the argument, χ . Citing the central limit theorem, it can be argued that both χ and ϕ are Gaussian random variables, in which case the associated Strehl distribution will be log-normal

$$p(S) \approx \frac{1}{\sqrt{2\pi} \sigma_I^2 S} \exp \left\{ -\frac{[\ln(S) - \langle \ln(S) \rangle]^2}{2\sigma_I^2} \right\} . \quad (6-3)$$

Since this approximation is generally only applicable when the mean Strehl is close to unity, its shape is specified primarily by the scintillation index, σ_I^2 . The relationship between σ_I^2 and the turbulence profile in the small-aperture limit was specified earlier in Eq. (5-4).

A representative set of comparisons between simulation results and the log-normal model is shown in Figure 6-1 for a case where the beam diameter is small compared to the coherence diameter ($w_0/r_0 = 0.0744$). The shape of the model functions is solely determined by the value of σ_I^2 , which is essentially identical for the uncorrected and tilt-corrected measurements in this example.

6.2 DISTRIBUTION MODEL FOR $w_0/r_0 \approx 1$: MODERATE NEAR-FIELD TURBULENCE

This case is the most difficult of the three to model due to the complex phenomenology in the transition region between the point-source and large-beam limits. For uncorrected turbulence, tilt-jitter becomes a dominant effect, and beam-breakup strongly influences the received signal fluctuations in systems that incorporate closed-loop track correction. For both of these system architectures, the shape of the irradiance distribution is found to be very different from the log-normal function that derives from the weak-turbulence approximation.

The essential constituent of the tilt-dominated distribution is the power-law model, which was introduced in Eq. (5-14). Unfortunately, this model does not adequately capture irradiance behavior near the distribution mean, because it does not include the effects of high spatial-frequency phase fluctuations in the transmitter plane. The approach taken in this section parallels the design of most adaptive-optics phase compensation systems in that the tilt and figure (tilt-removed phase) components of the near-field distortion are addressed separately.

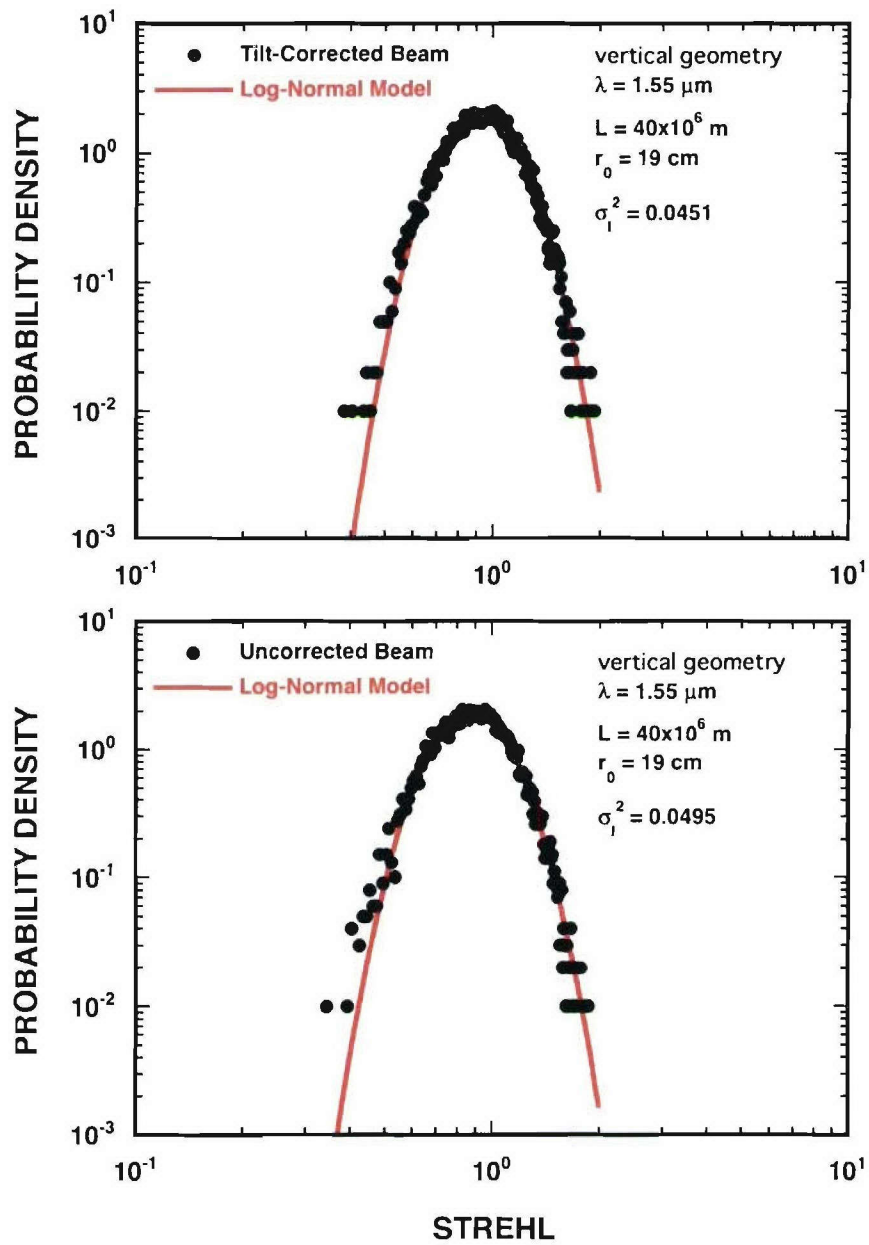


Figure 6-1. Comparison of uplink simulation results for $w_0/r_0 = 0.0744$ (black data points) with the log-normal distribution model (red line). The upper figure represents the tilt-corrected turbulence case and the lower is the uncorrected case.

The analytical treatment developed in this section relies heavily on a variation of the Nakagami- m distribution that is frequently used to characterize RF signal fading due to multipath [23,24]. The more familiar form of this expression describes the statistics of the field amplitude, but when written in terms of the optical irradiance, the following relationship is obtained

$$p(S) = \frac{m}{\Gamma(m) \langle S \rangle} \left(m \frac{S}{\langle S \rangle} \right)^{m-1} \exp \left\{ -m \frac{S}{\langle S \rangle} \right\} . \quad (6-4)$$

This representation, which is a variation of the gamma distribution [25], includes a power-law function that is dominant when S is small and an exponential term that defines the shape of the curve near the distribution mean. However, it is not possible to separately adjust the properties of these two functional components because both are constrained by the parameter, m .

A three-parameter model version of the Nakagami model was developed as part of this investigation. The goal was to retain the simplicity of the model, while introducing a third parameter that allows the shapes of the curves near the mean and the low-Strehl tail to be independently controlled. The derivation begins with the assumption that Eq. (5-14) can be generalized as follows

$$p(S) = \begin{cases} \frac{m}{S_0} (S/S_0)^{m-1} & : 0 \leq S \leq S_0 \\ 0 & : \text{elsewhere} \end{cases} , \quad (6-5)$$

where $S_0 \leq 1$ is the peak Strehl achievable when tracking errors are perfectly corrected. If the tilt-removed Strehl parameter is treated as a time-varying random variable, then Eq. (6-5) can be written as the marginal distribution

$$\begin{aligned} p(S) &= \int_S^\infty p(S; S_0) p(S_0) dS_0 = m S^{m-1} \int_S^\infty S_0^{-m} p(S_0) dS_0 \\ &\approx \frac{m}{\langle S_0 \rangle} \left(\frac{S}{\langle S_0 \rangle} \right)^{m-1} \int_S^\infty p(S_0) dS_0 \end{aligned} \quad (6-6)$$

The approximate form of Eq. (6-6) is valid if the standard deviation, σ_0 , of the variable S_0 is small compared to its mean. This results in a representation that is the product of distinct tilt and figure components.

In the previous section, it was demonstrated that weak far-field perturbations yield scintillation statistics that are accurately described by a log-normal distribution. However, simulations show that as the perturbations in the near field become stronger the statistics of the tilt-removed Strehl more closely

resemble a simple Gaussian. For a Gaussian distribution, the integral indicated in the previous expression is equivalent to the complementary error function

$$\int_S^{\infty} p(S_0) dS_0 = \frac{1}{2} \operatorname{erfc} \left\{ \frac{S_0 - \langle S_0 \rangle}{\sqrt{2} \sigma_0} \right\} . \quad (6-7)$$

Unfortunately, the error function is difficult to manipulate analytically, so it would be desirable to substitute a more tractable expression having comparable properties near the distribution mean. From a Taylor's series expansion centered on $\langle S_0 \rangle$, it can be shown that the complementary error function closely resembles the exponential expression

$$\frac{1}{2} \operatorname{erfc} \left\{ \frac{S_0 - \langle S_0 \rangle}{\sqrt{2} \sigma_0} \right\} \approx \exp \left\{ -\ln(2) \left(\frac{S_0}{\langle S_0 \rangle} \right)^{\beta} \right\} , \quad \text{where } \beta = \frac{\sqrt{2/\pi} \langle S_0 \rangle}{\ln(2) \sigma_0} . \quad (6-8)$$

This is equivalent to replacing the Gaussian distribution with a form of the Weibull distribution [25], specifically

$$\frac{1}{\sqrt{2\pi} \sigma_0} \exp \left\{ -\frac{(S_0 - \langle S_0 \rangle)^2}{2 \sigma_0^2} \right\} \approx \frac{\ln(2) \beta}{\langle S_0 \rangle} \left(\frac{S_0}{\langle S_0 \rangle} \right)^{\beta-1} \exp \left\{ -\ln(2) \left(\frac{S_0}{\langle S_0 \rangle} \right)^{\beta} \right\} . \quad (6-9)$$

The observations outlined above motivated the formulation of the following three-parameter scintillation model, which is referred to in this report as the modified Nakagami (or mod-N) distribution

$$p(S) = \frac{C \beta}{\Gamma(m/\beta) \langle S \rangle} \left(C \frac{S}{\langle S \rangle} \right)^{m-1} \exp \left\{ -\left(C \frac{S}{\langle S \rangle} \right)^{\beta} \right\} . \quad (6-10)$$

The constant $C \equiv \frac{\Gamma((m+1)/\beta)}{\Gamma(m/\beta)}$ has been defined to simplify the notation. Note that this result is equivalent to Eq. (6-4) when $\beta=1$, but that non-unity values of β provide a means to independently control the characteristics of the tilt-removed component of the expression. The moments of this function have a simple analytical form

$$\mu'_k = \frac{\Gamma((m+k)/\beta)}{\Gamma(m/\beta)} \left(\frac{\langle S \rangle}{C} \right)^k , \quad (6-11)$$

so the scintillation index can be expressed as

$$\sigma_I^2 = \frac{\Gamma((m+2)/\beta) \Gamma(m/\beta)}{\Gamma((m+1)/\beta)^2} - 1 \quad (6-12)$$

The integral of the probability density is the incomplete gamma function

$$P(S) = \int_0^S p(S') dS' = \frac{\gamma(m/\beta, (CS/\langle S \rangle)^\beta)}{\Gamma(m/\beta)} \quad (6-13)$$

Although the proposed model and its associated moments have a relatively simple mathematical structure, a strategy for computing the model parameters m and β is not immediately obvious. The following steps outline a straightforward process for developing estimates of both parameters given knowledge of the scintillation indices for uncorrected and tilt-corrected turbulence.

If one accepts the premise that the effects of the figure component of near-field phase errors can be modeled as a Weibull distribution, then the following result is derived

$$p_{fig}(S_0) = \frac{\Gamma(1/\beta)}{\langle S_0 \rangle} \left(\frac{\Gamma(1/\beta)}{\beta} \frac{S_0}{\langle S_0 \rangle} \right)^{\beta-1} \exp \left\{ - \left(\frac{\Gamma(1/\beta)}{\beta} \frac{S_0}{\langle S_0 \rangle} \right)^\beta \right\} \quad (6-14)$$

Note that this equation does not include the power-law parameter, m . Therefore, the scintillation index for the figure component is

$$\left[\sigma_I^2 \right]_{fig} = \frac{\Gamma(1+2/\beta)}{\Gamma(1+1/\beta)^2} - 1 \approx \beta^{-1/6} \quad (6-15)$$

where the approximation given in the second relationship is accurate when $\beta > 1$. This step establishes the value of β . An estimate of the power-law parameter, m , derives from Eq. (6-12)

$$\sigma_I^2 = \frac{\Gamma((m+2)/\beta) \Gamma(m/\beta)}{\Gamma((m+1)/\beta)^2} - 1 \approx \left(\frac{m}{\beta} \right)^{-(1+0.1\sqrt{\beta})} \beta^{-1/6} \quad (6-16)$$

where the approximate form provides an acceptable estimate when $m/\beta < 1$. If required, the accuracy of the estimates for the two shape parameters can be improved by inverting Eqs. (6-15) and (6-16) numerically.

The following three figures illustrate the evolution of the tilt-corrected and uncorrected irradiance distribution functions for increasing values of w_0/r_0 . All simulations incorporate the Hufnagel-Valley C_n^2 profile and vertical propagation. The log-normal model is included for comparison.

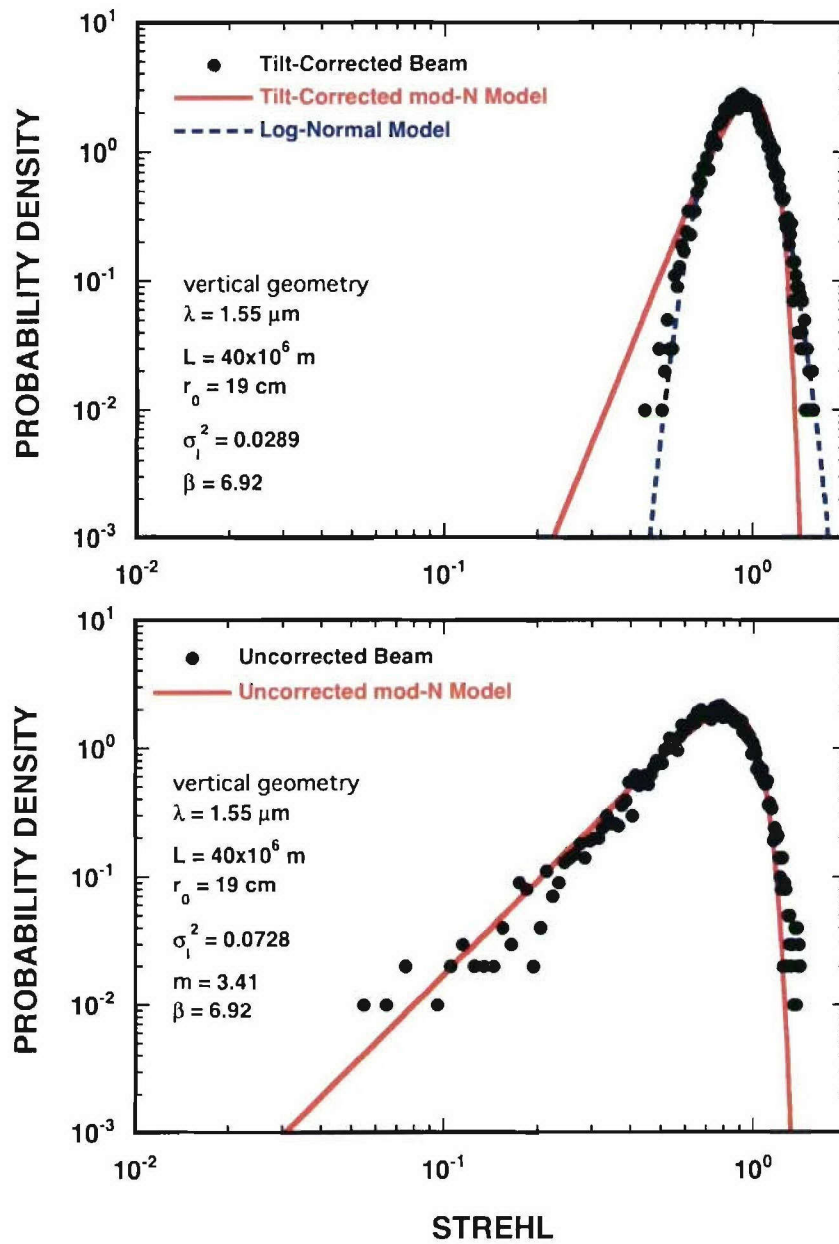


Figure 6-2. Comparison of uplink simulation results for $w_0/r_0 = 0.187$ (black data points) with the log-normal distribution model (red line). The upper figure represents the tilt-corrected turbulence case and the lower is the uncorrected case.

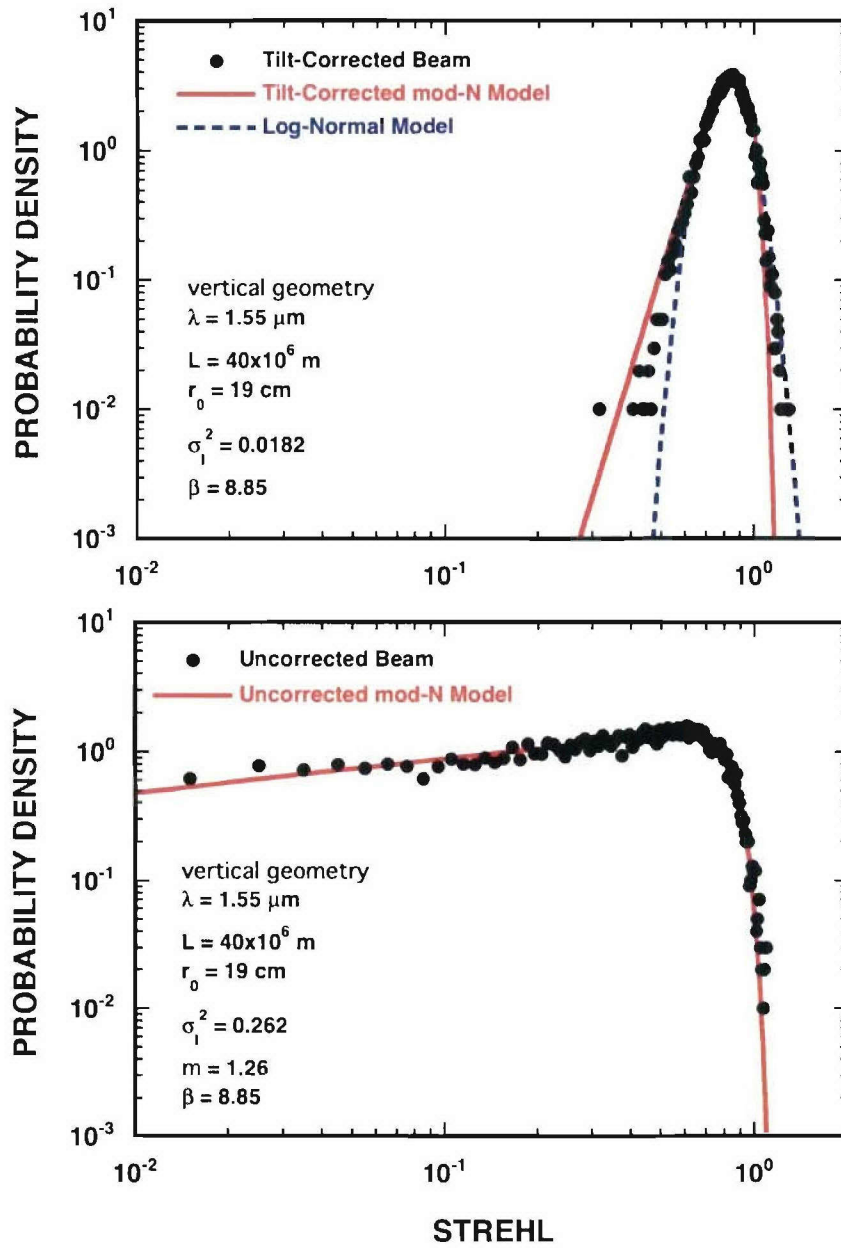


Figure 6-3. Comparison of uplink simulation results for $w_0/r_0 = 0.371$ (black data points) with the log-normal distribution model (red line). The upper figure represents the tilt-corrected turbulence case and the lower is the uncorrected case.

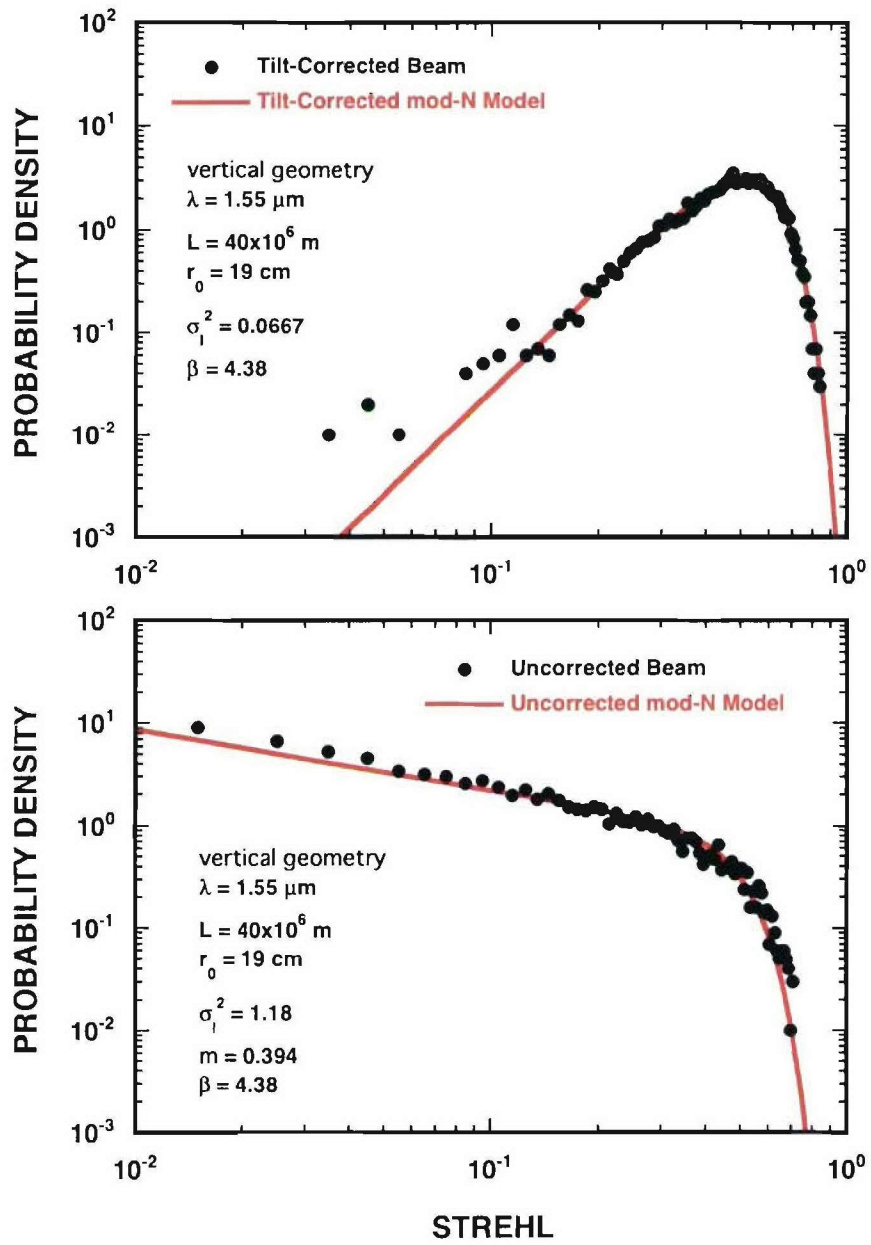


Figure 6-4. Comparison of uplink simulation results for $w_0/r_0 = 0.930$ (black data points) with the log-normal distribution model (red line). The upper figure represents the tilt-corrected turbulence case and the lower is the uncorrected case.

The previous examples demonstrate that the modified Nakagami model provides a very good fit to the uncorrected turbulence cases, but is less successful in matching the shapes of the distributions for tilt-corrected turbulence when w_0/r_0 is small. In the latter case, the log-normal distribution is clearly superior, presumably because the relative contribution of far-field turbulence is significant. A method for combining the log-normal and modified Nakagami functions is described in Section 6.4.

6.3 DISTRIBUTION MODEL FOR $w_0/r_0 \gg 1$: SATURATION DUE TO STRONG NEAR-FIELD TURBULENCE

In the discussions relating to saturated scintillation presented in Section 5, it was noted that this condition appears to be associated with near-field distortions that are strong enough to create a uniform distribution of phase errors within the range of $\pm\pi$. In this limit, the field in the transmitter plane can be modeled as an ensemble of N independent emitters, where $N \approx 1/\langle S \rangle$. The resulting distribution is the single-parameter negative-exponential function

$$p(S) = \frac{1}{\langle S \rangle} \exp \left\{ -\frac{S}{\langle S \rangle} \right\} . \quad (6-17)$$

This is a special case of the Weibull distribution given in Eq. (6-14) for which the shape parameter, β , is equal to 1, and is also a special case of the modified Nakagami function with $m = \beta = 1$. A distinguishing characteristic of negative exponential distribution is that the function approaches a constant for small values of S .

The scintillation index for this distribution is unity, and the shape of the curve is entirely determined by the mean Strehl, $\langle S \rangle$. In the saturation limit, the mean Strehl can be estimated from Eq. (5-38)

$$\langle S \rangle \approx 0.125 (w_0/r_0)^{-2} , \quad (6-18)$$

which indicates that the number of equivalent incoherent emitters is proportional to the number of coherence-diameter regions within the profile of the transmitted beam.

A representative example of the irradiance distribution for saturated scintillation is given in Figure 6-5. The shapes of the curves for tilt-corrected and uncorrected turbulence are nearly identical and are solely determined by the value of the mean Strehl. It is interesting to note, however, that the uncorrected-turbulence plots in both Figure 6-4 and 6-5 show evidence of a slightly-negative power law exponent (i.e., $m < 1$). This condition appears to coincide with the region of overshoot in the scintillation index function shown in Figure 5-6 and may be the result of beam tilt fluctuations that exceed the short-exposure beam radius.

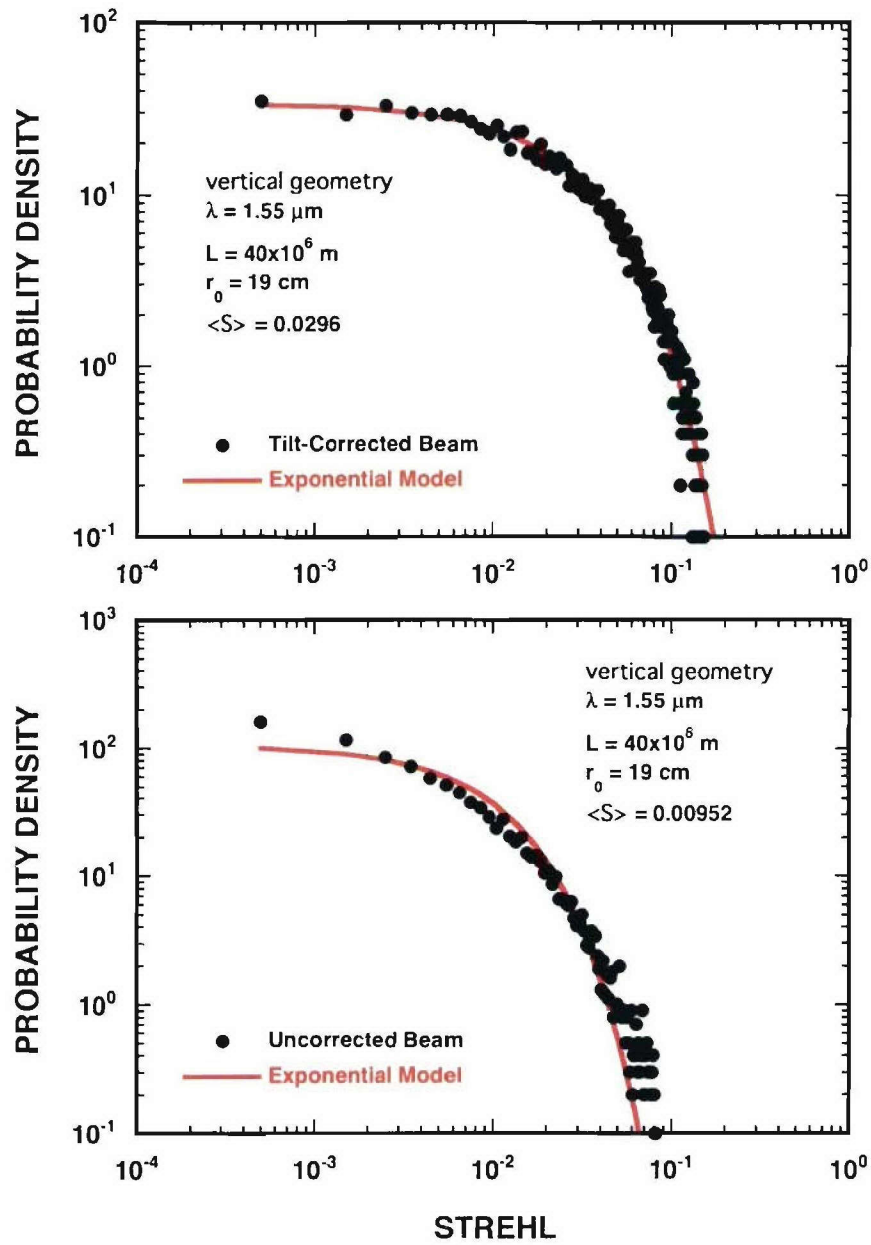


Figure 6-5. Comparison of uplink simulation results for $w_0/r_0 = 3.72$ (black data points) with the negative-exponential distribution model (red line). The upper figure represents the tilt-corrected turbulence case and the lower is the uncorrected case.

6.4 COMBINING THE IRRADIANCE DISTRIBUTION MODELS

The statistical models discussed in the last two sections are appropriate for disturbances confined primarily to the near-field of the transmitter, and they all represent variations of the three-parameter function that has been referred to in this report as the modified Nakagami distribution. Far-field phase perturbations, on the other hand, result in signal distributions that closely resemble a two-parameter log-normal function. A formalism that achieves a smooth transition between these two dissimilar representations is presented in this section.

A review of the tilt-corrected simulation data that appears in Figures 6-2 and 6-3 provide a good starting point for this discussion. In the first example, the data are closely matched to the log-normal function, whereas in the second case the simulation results in the tail of the distribution fall between the estimates provided by the near- and far-field scintillation models. In both cases, the modified Nakagami distribution overestimates the likelihood of a deep fade, although it could be argued that this discrepancy is typically not important when the scintillation index is small. However, for communication systems designed to operate near the link margin, a higher degree of prediction accuracy may be needed.

The approach proposed for combining the near- and far-field scintillation models derives from the discussion of the composite scintillation index provided in Section 5.5. The following expression represents a weighted average of the two distributions

$$p(S) = \frac{\left[\sigma_I^2\right]_{FF}^2 p_{FF}(S) + \left[\sigma_I^2\right]_{NF}^2 p_{NF}(S)}{\left[\sigma_I^2\right]_{FF}^2 + \left[\sigma_I^2\right]_{NF}^2}, \quad (6-19)$$

where the values of the weights are specified by the scintillation indices as defined in Eqs. (5-29) through (5-32). The far- and near-field functions, p_{FF} and p_{NF} , refer to the log-normal and modified Nakagami distributions defined in Eqs. (6-3) and (6-10). The linear addition indicated in the last expression preserves both the statistical mean and variance of the two component distributions.

The effect of the composite distribution model is most significant in the region where the far-field and near-field contributions are comparable. In Figure 6-6, new plots of the tilt-removed data shown earlier in Figures 6-2 and 6-3 are given along with the composite model shown in the dashed green curve. In the former case, the composite model essentially replicates the log-normal model since far-field effects dominate, but in the second example it provides a significantly better match to the simulation output than either of the component distribution functions.

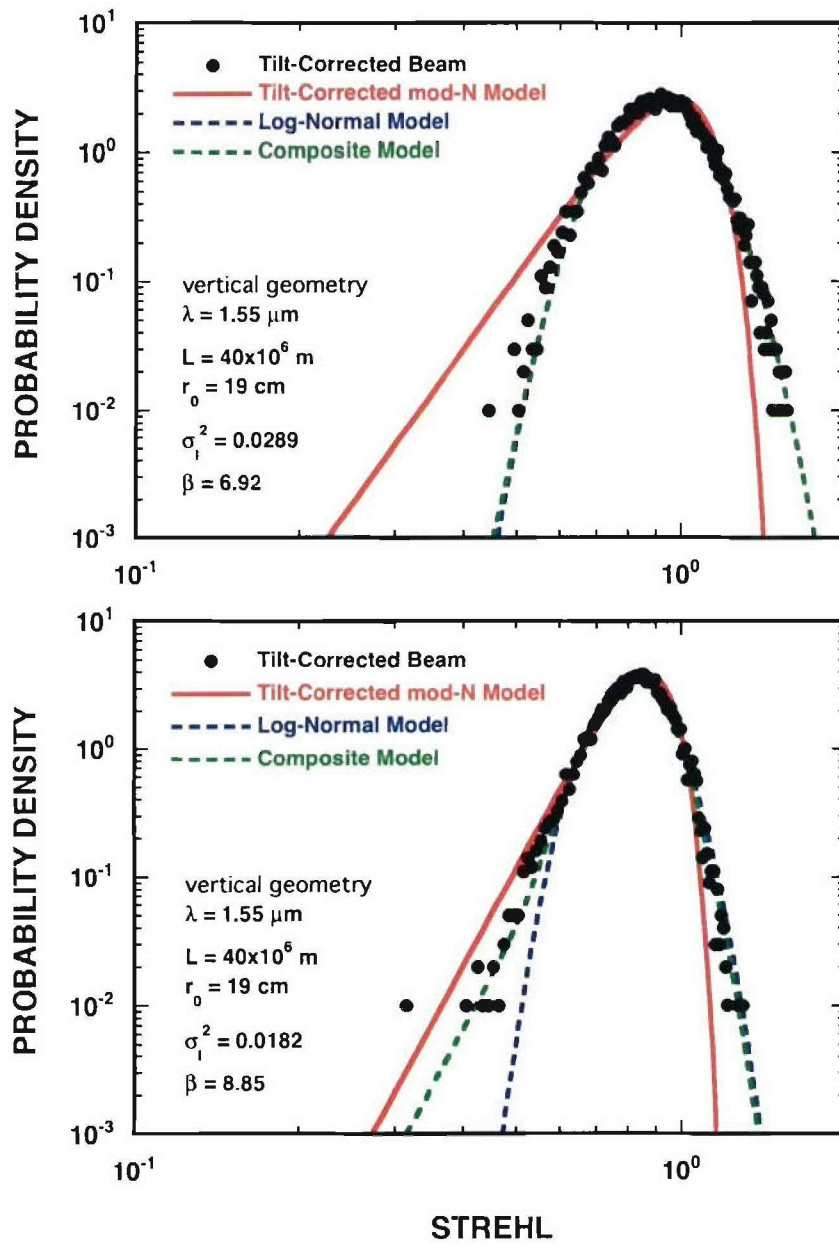


Figure 6-6. Comparison of uplink simulation results for the tilt-corrected beam (black data points) with the composite distribution model (green line). The upper figure represents the $w_0/r_0 = 0.187$ case and the lower is the result for $w_0/r_0 = 0.371$.

7. CONCLUSIONS

Numerical simulations of beamwave propagation frequently reveal significant discrepancies between the scintillation properties of the computational output and predictions based on the Rytov theory. This problem has frequently been encountered in studies of engagement geometries of practical interest, including many that are relevant to free-space optical communications. System designers are now requesting models that more accurately predict channel behavior, but which are also simple enough to allow their integration into high-level engineering software. The relationships developed in this report represent an attempt to satisfy both of those requirements.

Analytical investigations of weak scintillation have generally been restricted to two cases that can be solved through the use of the Rytov approximation—propagation of an infinite plane wave and illumination from a point source. Neither of these geometries is an adequate representation of a transceiver link that transmits a beam of finite dimensions, and which imparts a focus that is matched to the receiver range. Both of these propagation constraints are fundamental to most systems of practical interest, and both have been applied in this analysis.

One of the primary goals of this study is a much better understanding of the physical processes that drive receiver-plane signal fluctuations. Two parameters are found to be of particular importance. The first is the ratio between the outgoing beam diameter and the turbulence coherence diameter; this result is not unexpected in that this ratio appears frequently in publications dealing with turbulence effects and adaptive optics. The second factor, which is somewhat more subtle, is the relationship between locations of the individual perturbation planes and the Rayleigh range of the transmitted beam. This study has identified a fundamental difference between the effects of phase distortions introduced in the near field of the transmitter (within the Rayleigh range) and the far field (beyond the Rayleigh range). In general, near-field perturbations are not well characterized by predictions based on the Rytov approximation. This observation is particularly important for applications such as uplink communications, which exhibit a strong near-field component.

This report provides a practical approach to predicting irradiance statistics given knowledge of the beam size, propagation geometry, and turbulence profile. Although the relationships derived have thus far only been validated for the cases of vertical uplink and horizontal propagation, it is believed that they can be accurately applied to a much wider range of engagement geometries.

APPENDIX

The following derivation represents an alternative approach to the estimation of the scintillation index due to far-field perturbations and is intended to support the result developed in Section 5.1. As in the previous discussion, it is assumed that the primary effect of phase distortions close to the receiver plane is to modify the local curvature of the propagating wavefront. In essence, the physical model is that the beam propagates through a succession of concave and convex lenses before being intercepted by the receiver.

To obtain a quantitative description of the irradiance changes that result from the focus-driven model proposed above, the focus perturbation term, ε , will first be defined such that the effective field curvature in the z_1 plane is

$$\frac{1}{f_1'} = \frac{1}{z_1} (1 + \varepsilon) . \quad (\text{A-1})$$

The perturbed beam diameter in the z_2 plane further along the propagation path is

$$d_2' = d_2 + d_1 \left(\frac{1}{f_1'} - \frac{1}{z_1} \right) (z_2 - z_1) = d_2 + \varepsilon \frac{d_1}{z_1} (z_2 - z_1) , \quad (\text{A-2})$$

and the modified boresight irradiance is

$$I_2' = \frac{I_2}{\left[1 + \varepsilon d_1 (z_2 - z_1) / d_2 z_1 \right]^2} = \frac{I_2}{\left[1 + \varepsilon (z_2 - z_1) / z_2 \right]^2} \approx I_2 \left[1 - 2 \varepsilon (z_2 - z_1) / z_2 \right] . \quad (\text{A-3})$$

At this point the assumption will be made that ε is a zero-mean Gaussian random variable with variance σ_ε^2 . If the value of this parameter can be related to the turbulence strength at z_1 , then the statistics of I_2 are easily derived from Equation (A-3). Noll's article [11] shows that within a circular aperture of diameter d , the focus component of the phase error is

$$\left[\sigma_\phi^2 \right]_{\text{focus}} = 0.023 \left(\frac{d}{r_0} \right)^{5/3} = 0.0097 d^{5/3} k^2 C_n^2(z) \Delta z , \quad (\text{A-4})$$

where Δz is the phase-screen depth. For a wavefront characterized by the curvature radius, f , the piston and tilt-removed phase variance within the circle is [8]

$$\left[\sigma_{\phi}^2 \right]_{\text{focus}} = \frac{k^2 d^4}{768 f^2} . \quad (\text{A-5})$$

In this context the parameter, $y = 1/f^2$, can be regarded as a statistical quantity with expectation value

$$\langle y \rangle = \frac{768}{k^2 d^4} \left[\sigma_{\phi}^2 \right]_{\text{focus}} . \quad (\text{A-6})$$

If $x = 1/f$ is a zero-mean Gaussian variable, then the distribution for y is the gamma function

$$p(y) = \frac{1}{2\sqrt{2\pi} \sigma_x} y^{-1/2} \exp\left\{-\frac{y}{2\sigma_x^2}\right\} ,$$

which has the mean value, $\langle y \rangle = \sigma_x^2$. This provides the key relationship between the variance of $1/f$ and the focus component of the phase variance given in Equation (A-6). When this result is applied to the perturbation term in Equation (A-1) and combined with the expression for the characteristic radius developed in Section 4.3

$$d_1 = 2^{3/2} w_{\ell} = \sqrt{\frac{8 z_1 (z_2 - z_1)}{k z_2}} , \quad (\text{A-7})$$

it can be seen that

$$\sigma_{\varepsilon}^2 \approx \frac{768 z_1^2}{k^2 d_1^4} \left[\sigma_{\phi}^2 \right]_{\text{focus}} \approx 7.45 z_1^2 d_1^{-7/3} C_n^2(z_1) \Delta z \approx 0.66 k^{7/6} z_1^{5/6} \left(\frac{z_2}{z_2 - z_1} \right)^{7/6} C_n^2(z_1) \Delta z . \quad (\text{A-8})$$

The final step of the derivation incorporates the relationship between I_2 and ε given in Equation (A-3) to develop an expression for the receiver-plane intensity variance

$$\sigma_I^2 \approx 2.64 k^{7/6} z_1^{5/6} \left(\frac{z_2 - z_1}{z_2} \right)^{5/6} C_n^2(z_1) \Delta z . \quad (\text{A-9})$$

The variance for the entire propagation path derives from the assumption that the phase perturbations are additive and independent

$$\sigma_I^2 = 2.64 k^{7/6} \int_0^{z_2} z^{5/6} \left(\frac{z_2 - z}{z_2} \right)^{5/6} C_n^2(z) dz \quad . \quad (\text{A-10})$$

The leading constant in this result differs from the standard expression given in Equation (5-3) by about 20%, but this qualitative agreement tends to support the argument that the primary effect of far-field perturbations is embodied in a model that describes far-field perturbations as a series of thin lenses.

REFERENCES

1. J. W. Goodman, *Statistical Optics*, John Wiley & Sons (1985).
2. A. N. Kolmogorov, "Dissipation of Energy in Locally Isotropic Turbulence," *Doklady Akad. Nauk. SSSR*, vol. 32, p. 16 (1941).
3. V. I. Tatarski, *Wave Propagation in a Turbulent Medium*, McGraw-Hill Book Company, Inc., New York (1961).
4. A. Ishimaru, *Wave Propagation and Scattering in Random Media*, Vols. 1 and 2, Academic Press, New York (1978).
5. J. W. Strohbehn, *Laser Beam Propagation in the Atmosphere*, Springer-Verlag, Berlin (1978).
6. D. L. Fried, "Optical Resolution Through a Randomly Inhomogeneous Medium for Very Long and Very Short Exposures," *J. Opt. Soc. Am.*, vol. 56, p. 1372 (1966).
7. H. T. Yura, "Short-Term Average Optical-Beam Spread in a Turbulent Medium," *J. Opt. Soc. Am.*, vol. 63, p. 567 (1973).
8. R. J. Sasiela, *Electromagnetic Wave Propagation in Turbulence*, Springer-Verlag (1994).
9. D. L. Fried, "Limiting Resolution Looking Down Through the Atmosphere," *J. Opt. Soc. Am.*, vol. 56, p. 1380 (1966).
10. M. I. Charnotskii, "Asymptotic Analysis of Finite-Beam Scintillations in a Turbulent Medium," *Waves in Random Media*, 4, 243 (1994).
11. R. J. Noll, "Zernike Polynomials and Atmospheric Turbulence," *J. Opt. Soc. Am.*, vol. 66, p. 207 (1976).
12. J. W. Goodman, *Introduction to Fourier Optics*, McGraw-Hill Book Co. (1968).
13. L. C. Andrews and R. L. Phillips, *Laser Beam Propagation through Random Media*, SPIE Optical Engineering Press, Bellingham (1998).
14. B. J. Herman and L. A. Strugala, "Method for Inclusion of Low-Frequency Contributions in Numerical Representation of Atmospheric Turbulence," *SPIE*, vol. 1221, 183-192 (1990).
15. V. I. Talanov, "Focusing of Light in Cubic Media," *JETP Letters*, vol. 11, p. 199 (1970).

16. R. E. Hufnagel, *The Infrared Handbook* (edited by W. L. Wolfe and G. J. Zeiss), Environmental Research Institute of Michigan (1978).
17. D. L. Fried, "Statistics of Laser Beam Fade Induced by Pointing Jitter," *Applied Optics*, vol. 12, p. 422 (1973).
18. P. J. Titterton, "Power Reduction and Fluctuations Caused by Narrow Laser Beam Motion in the Far Field," *Applied Optics*, vol. 12, p. 423 (1973).
19. V. A. Banakh and I. N. Smalikho, "Statistical Characteristics of the Laser Beam Propagation Along Vertical and Sloping Paths through a Turbulent Atmosphere," *SPIE*, vol. 1968, 303-311 (1993).
20. G. J. Baker, "Gaussian Beam Weak Scintillation: a Tour of the D_1 Region," *SPIE*, vol. 5793, 17-27 (2005).
21. P. Beckmann, *Probability in Communication Engineering*, Harcourt, Brace, and World, Inc. (1967).
22. L. C. Andrews, R. L. Phillips, and C. Y. Hopen, *Laser Beam Scintillation with Applications*, SPIE Optical Engineering Press, Bellingham (2001).
23. M. K. Simon and M. Alouini, *Digital Communication over Fading Channels*, John Wiley & Sons, Inc. (2000).
24. J. G. Proakis, *Digital Communications*, McGraw-Hill (1995).
25. K. Bury, *Statistical Distributions in Engineering*, Cambridge University Press (1999).

REPORT DOCUMENTATION PAGE

Form Approved
OMB No. 0704-0188

Public reporting burden for this collection of information is estimated to average 1 hour per response, including the time for reviewing instructions, searching existing data sources, gathering and maintaining the data needed, and completing and reviewing this collection of information. Send comments regarding this burden estimate or any other aspect of this collection of information, including suggestions for reducing this burden to Department of Defense, Washington Headquarters Services, Directorate for Information Operations and Reports (0704-0188), 1215 Jefferson Davis Highway, Suite 1204, Arlington, VA 22202-4302. Respondents should be aware that notwithstanding any other provision of law, no person shall be subject to any penalty for failing to comply with a collection of information if it does not display a currently valid OMB control number. **PLEASE DO NOT RETURN YOUR FORM TO THE ABOVE ADDRESS.**

1. REPORT DATE (DD-MM-YYYY) 12 December 2005		2. REPORT TYPE Technical Report		3. DATES COVERED (From - To)										
4. TITLE AND SUBTITLE Distribution Models for Optical Scintillation Due to Atmospheric Turbulence				5a. CONTRACT NUMBER FA8721-05-C-0002										
				5b. GRANT NUMBER										
				5c. PROGRAM ELEMENT NUMBER										
6. AUTHOR(S) Ronald R. Parenti and Richard J. Sasiela				5d. PROJECT NUMBER 1										
				5e. TASK NUMBER 98124										
				5f. WORK UNIT NUMBER										
7. PERFORMING ORGANIZATION NAME(S) AND ADDRESS(ES) MIT Lincoln Laboratory 244 Wood Street Lexington, MA 02420-9108				8. PERFORMING ORGANIZATION REPORT NUMBER TR-1108										
9. SPONSORING / MONITORING AGENCY NAME(S) AND ADDRESS(ES) ESC/XPI				10. SPONSOR/MONITOR'S ACRONYM(S)										
				11. SPONSOR/MONITOR'S REPORT NUMBER(S) ESC-TR-2005-070										
12. DISTRIBUTION / AVAILABILITY STATEMENT Approved for public release; distribution is unlimited.														
13. SUPPLEMENTARY NOTES														
14. ABSTRACT Traditional analyses of optical scintillation usually invoke the Rytov approximation and the associated assumptions regarding weak phase perturbations throughout the propagation channel. Associated with that approach is the prediction that the statistics of scintillation will be log-normal. This report, which uses the Fresnel propagation function as a basis, challenges many of the standard descriptions of far-field irradiance fluctuations. A key finding of this study is the importance of the ratio between the transmitted beam diameter and the turbulence coherence diameter. Turbulence-induced beam jitter is found to be a dominant effect when this radius is close to unity, and the relationship between pointing error and scintillation is examined in detail. As a result of this work, models for the mean Strehl, scintillation index, and signal-fade distributions have been developed. Included in this document are a set of detailed comparisons between the new theoretical models and numerical results derived from a beamwave propagation code developed by Lincoln Laboratory.														
15. SUBJECT TERMS <table border="0"> <tr> <td>atmospheric turbulence</td> <td>Rytov approximation</td> <td>Strehl ratio</td> </tr> <tr> <td>fade probability</td> <td>scintillation</td> <td>tilt correction</td> </tr> <tr> <td>fading channel</td> <td>scintillation index</td> <td></td> </tr> </table>						atmospheric turbulence	Rytov approximation	Strehl ratio	fade probability	scintillation	tilt correction	fading channel	scintillation index	
atmospheric turbulence	Rytov approximation	Strehl ratio												
fade probability	scintillation	tilt correction												
fading channel	scintillation index													
16. SECURITY CLASSIFICATION OF:			17. LIMITATION OF ABSTRACT	18. NUMBER OF PAGES	19a. NAME OF RESPONSIBLE PERSON									
a. REPORT Unclassified	b. ABSTRACT Unclassified	c. THIS PAGE Unclassified			19b. TELEPHONE NUMBER (include area code)									
			None	76										